Article

Optimizing Landsat Next Shortwave Infrared Bands for Crop Residue Characterization

Brian T. Lamb [1,*], Philip E. Dennison [2], W. Dean Hively [3], Raymond F. Kokaly [4], Guy Serbin [5], Zhuoting Wu [6], Philip W. Dabney [7], Jeffery G. Masek [7], Michael Campbell [2] and Craig S. T. Daughtry [8]

1 U.S. Geological Survey, Lower Mississippi-Gulf Water Science Center, Coram, NY 11727, USA
2 Department of Geography, University of Utah, Salt Lake City, UT 84112, USA
3 U.S. Geological Survey, Lower Mississippi-Gulf Water Science Center, Beltsville, MD 20705, USA
4 U.S. Geological Survey, Geology, Geophysics, and Geochemistry Science Center, Lakewood, CO 80225, USA
5 Mallon Technology Ltd., Suite 403, 34 Fitzwilliam Square, D02 X840 Dublin, Ireland
6 U.S. Geological Survey, Office of Land Remote Sensing, Flagstaff, AZ 86001, USA
7 NASA Goddard Space Flight Center, Biospheric Sciences Laboratory, 8800 Greenbelt Road, Greenbelt, MD 20771, USA
8 Agricultural Research Service, Hydrology and Remote Sensing Laboratory, U.S. Department of Agriculture, Beltsville, MD 20705, USA
* Correspondence: blamb@usgs.gov

Abstract: This study focused on optimizing the placement of shortwave infrared (SWIR) bands for pixel-level estimation of fractional crop residue cover (f_R) for the upcoming Landsat Next mission. We applied an iterative wavelength shift approach to a database of crop residue field spectra collected in Beltsville, Maryland, USA (n = 916) and computed generalized two- and three-band spectral indices for all wavelength combinations between 2000 and 2350 nm, then used these indices to model field-measured f_R. A subset of the full dataset with a Normalized Difference Vegetation Index (NDVI) < 0.3 threshold (n = 643) was generated to evaluate green vegetation impacts on f_R estimation. For the two-band wavelength shift analyses applied to the NDVI < 0.3 dataset, a generalized normalized difference using 2226 nm and 2263 nm bands produced the top f_R estimation performance (R^2 = 0.8222; *RMSE* = 0.1296). These findings were similar to the established two-band Shortwave Infrared Normalized Difference Residue Index (SINDRI) (R^2 = 0.8145; *RMSE* = 0.1324). Performance of the two-band generalized normalized difference and SINDRI decreased for the full-NDVI dataset (R^2 = 0.5865 and 0.4144, respectively). For the three-band wavelength shift analyses applied to the NDVI < 0.3 dataset, a generalized ratio-based index with a 2031–2085–2216 nm band combination, closely matching established Cellulose Absorption Index (CAI) bands, was top performing (R^2 = 0.8397; *RMSE* = 0.1231). Three-band indices with CAI-type wavelengths maintained top f_R estimation performance for the full-NDVI dataset with a 2036–2111–2217 nm band combination (R^2 = 0.7581; *RMSE* = 0.1548). The 2036–2111–2217 nm band combination was also top performing in f_R estimation (R^2 = 0.8690; *RMSE* = 0.0970) for an additional analysis assessing combined green vegetation cover and surface moisture effects. Our results indicate that a three-band configuration with band centers and wavelength tolerances of 2036 nm ($\pm$5 nm), 2097 nm ($\pm$14 nm), and 2214 ($\pm$11 nm) would optimize Landsat Next SWIR bands for f_R estimation.

Keywords: Landsat Next; crop residue; non-photosynthetic vegetation; tillage; lignocellulose; shortwave infrared; CAI; SINDRI; LCPCDI; NDTI; NDVI; SWIR

1. Introduction

The Landsat Next satellite, scheduled for launch at the end of this decade, is expected to provide multispectral imagery at spatial resolutions of 10 m to 20 m [1,2]. Increases in the number of bands and finer spatial resolutions compared to previous Landsat missions (multispectral imagery at 30 m) will advance remote sensing-based studies in many fields

including agriculture, ecology, forestry, hydrology, and minerology. In this research effort, we focus on Landsat Next capabilities in characterizing non-photosynthetic vegetation (NPV) which has critical applications in agricultural and ecological studies. An important type of NPV is crop residue, namely the NPV that remains on agricultural fields post-harvest. Agricultural fields that are managed with higher levels of fractional crop residue cover (f_R) are less prone to erosion, have greater soil organic carbon, and more stable soil moisture [3–6]. The amount of f_R on fields also serves as an important indicator of tillage intensity, particularly when measured in late spring immediately after the planting of summer crops [7,8].

In past Landsat missions, a shortwave infrared (SWIR) spectral region spanning 2000–2500 nm (sometimes referred to as "SWIR2") has been measured by a single band [9]. The SWIR2 band spanned approximately 2080 to 2350 nm for Landsat 4 and 5 Thematic Mapper (TM) and Landsat 7 Enhanced Thematic Mapper+ (ETM+) [10]. A single SWIR2 band is still used for Landsat 8 and 9 Operational Land Imagers (OLI and OLI2, respectively) but has a narrowed spectral response (approximately 2110 to 2290 nm). Similarly, the Sentinel-2 MultiSpectral Instruments (MSI) use a single SWIR2 band, approximately 2100 to 2280 nm. Use of a single SWIR2 band in global Earth resource monitoring missions limits the spectral separation of NPV from soils, green vegetation, and other land cover types, even when using approaches comparing SWIR2 reflectance to SWIR1 reflectance [1,11]. SWIR1, spanning 1400–1850 nm, is also covered by a single band centered at approximately 1610 nm [12].

Over the past 30 years, the lignin and cellulose (lignocellulose) absorption features centered near 2100 nm and 2300 nm have been exploited by applying imaging spectrometer data to NPV detection and characterization [13–17]. Some of these imaging spectrometers/missions include the Airborne Visible/Infrared Imaging Spectrometer (AVIRIS), Earth Observing One (EO-1) Hyperion, and *PRecursore IperSpettrale della Missione Applicativa* (PRISMA). To date, both airborne and spaceborne imaging spectrometers have been limited in coverage, e.g., swath footprint and revisit intervals. Narrow band multispectral imagers with multiple SWIR bands, like those on the WorldView-3 (WV3), also offer capabilities in resolving lignocellulose absorption features, but, like spaceborne and airborne imaging spectrometers, are limited in coverage. In comparison, current imaging systems with global coverage and regular revisit intervals, such as sensors on Landsat and Sentinel-2, have limited capabilities in resolving lignocellulose absorption features due to poor SWIR sampling by broad band sensors, e.g., SWIR2. To better resolve the lignocellulose absorption features present in NPV, Landsat Next's imaging system is expected to feature regular global coverage and three relatively narrow bands covering the heritage SWIR2 spectral region. Figure 1 provides a depiction of potential Landsat Next SWIR band placements compared to ETM+, OLI, MSI, WV3, and spectrometer data with similar spectral sampling as hyperspectral AVIRIS and PRISMA bands.

Despite band width limitations, f_R estimates have, at times, been provided by Landsat/Sentinel-2 satellites with global coverage [18–22]. In some of the most successful regional-scale crop residue studies incorporating Landsat/Sentinel-2 SWIR imagery, the accuracy assessing broad categories of f_R and associated tillage intensity generally ranges between 55 and 79% and requires the use of regionally-specific approaches [22–24]. Well-calibrated, site-specific studies utilizing Landsat/Sentinel-2 SWIR bands may offer higher accuracies in f_R estimation (>80%). In general, both regional-scale and site-specific crop residue studies using Landsat/Sentinel-2 imagery make use of spectral indices computed from SWIR2 and SWIR1 bands like the Normalized Difference Tillage Index (NDTI) [18,20]. While site-specific studies using NDTI to estimate f_R can achieve fairly high accuracies, high levels of inter-site variability in NDTI values for fixed f_R values make such indices ill-suited for global mapping efforts [19–21]. Site-specific studies incorporating spectral angle mapping (SAM) from Landsat/Sentinel-2 bands have demonstrated some of the highest levels of performance in f_R estimation (>90%) [25,26]. Additionally, South et al. (2004) [27] demonstrated that SAM consistently outperformed statistical classification approaches

when using Landsat imagery to classify tillage intensity categories (>92% vs. <72%). However, it remains unclear how effectively such approaches can be scaled regionally or globally, as no such large-scale studies have been carried out to our knowledge, and current SAM approaches are ultimately reliant on spectrally broad reflectance contrasts that may lack sufficient biophysical specificity, e.g., near infrared—SWIR1—SWIR2 comparisons.

For f_R estimation, finer spectral resolution data sources offer improved accuracies over coarser resolution data sources since the later cannot accurately detect lignocellulose absorption features at 2100 and 2300 nm [11,20,28] (Figure 1). Finer spectral resolution data sources are particularly suited for application of spectral unmixing for f_R estimation when there is a preponderance of mixed pixels containing f_R, fractional soil (f_S), and fractional green vegetation (f_{GV}) that result from different field management practices like tillage and planting. Bannari et al. (2006) [28] provide an illustrative comparison of spectral unmixing approaches applied to hyperspectral and broad band multispectral data sources, with the former yielding higher accuracies in f_R estimation. Daughtry et al. (2006) [11] provide a similar hyperspectral vs. broad band multispectral comparison using spectral index approaches, demonstrating higher f_R estimation performance for hyperspectral indices with R^2 ranging from 0.774 to 0.850 while broad band indices R^2 ranged from 0.108 to 0.498. Yue et al. (2019) [29] provide a comparison of both hyperspectral indices and SAM approaches compared to broad band multispectral indices, demonstrating that both hyperspectral approaches outperform broad band multispectral indices in laboratory-based f_R estimation. Multispectral imagery with narrow-to-moderate band widths (<60 nm) offers similar improvements in f_R estimation accuracy compared to broad band multispectral data sources. Hively et al. (2018) [20] demonstrated performance differences between narrow band multispectral SWIR indices derived from WV3 imagery compared to Landsat-simulated SWIR indices derived from convolved WV3 bands, with the former exhibiting f_R estimation performance improvements of 10% or greater under conditions of minimal f_{GV} and minimal surface moisture variability. In f_R estimation studies where significant f_{GV} is present or surface moisture is highly variable, finer spectral resolution imagery vastly outperforms heritage Landsat SWIR bands [30–32].

The prior paragraphs convey a critical limitation for accurate spaceborne monitoring of crop residue and associated agricultural tillage: few current satellites possess the optimal characteristics for retrieving f_R including regular revisit cadence, global coverage, fine spatial resolution, and fine spectral resolution in the SWIR2 region. These current limitations and future satellite needs extend beyond conventional agricultural applications as accurate characterization of fractional NPV cover (f_{NPV}) is critical in the assessment of wild vegetation health, drought condition, and rangeland forage quality [33–36]. Although our study focused on f_R assessment for agricultural applications, many of our findings could be broadly applicable to non-agricultural f_{NPV} assessment as well.

An initial evaluation of prospective Landsat Next SWIR bands for f_R and f_{NPV} characterization was carried out by Hively et al. (2021) [37] using established spectral band locations from satellite missions including Advanced Spaceborne Thermal Emission and Reflection Radiometer (ASTER), Hyperion, and WV3, in addition to heritage Landsat bands. These bands are shown in Figure 1. This previous study found that narrow bands positioned near lignocellulose absorption features were substantially more accurate in f_R estimation than heritage Landsat bands (R^2 of 0.81 and 0.77, respectively, for two-band and three-band indices, compared to R^2 of 0.44 for Landsat heritage indices). In the current research effort, we sought to improve upon the evaluation of previous band locations by implementing an iterative wavelength shift approach that assesses f_R estimation capabilities across all band combinations in the portions of the SWIR most relevant to crop residue characterization (2000–2350 nm) [38]. We evaluated f_R estimation error using spectral indices based on two- and three-band combinations covering the SWIR2 region. After identifying the top-performing spectral bands using the iterative wavelength shift approach, we assessed how well these wavelengths performed in f_R estimation under conditions of variable surface moisture and f_{GV} presence compared to the wavelengths of

established crop residue indices. Ideally, the findings of this research effort will be useful for further informing SWIR band placements for the Landsat Next mission and developing a methodology useful for generalized spectral band selections for biophysical variables pertinent to other application areas.
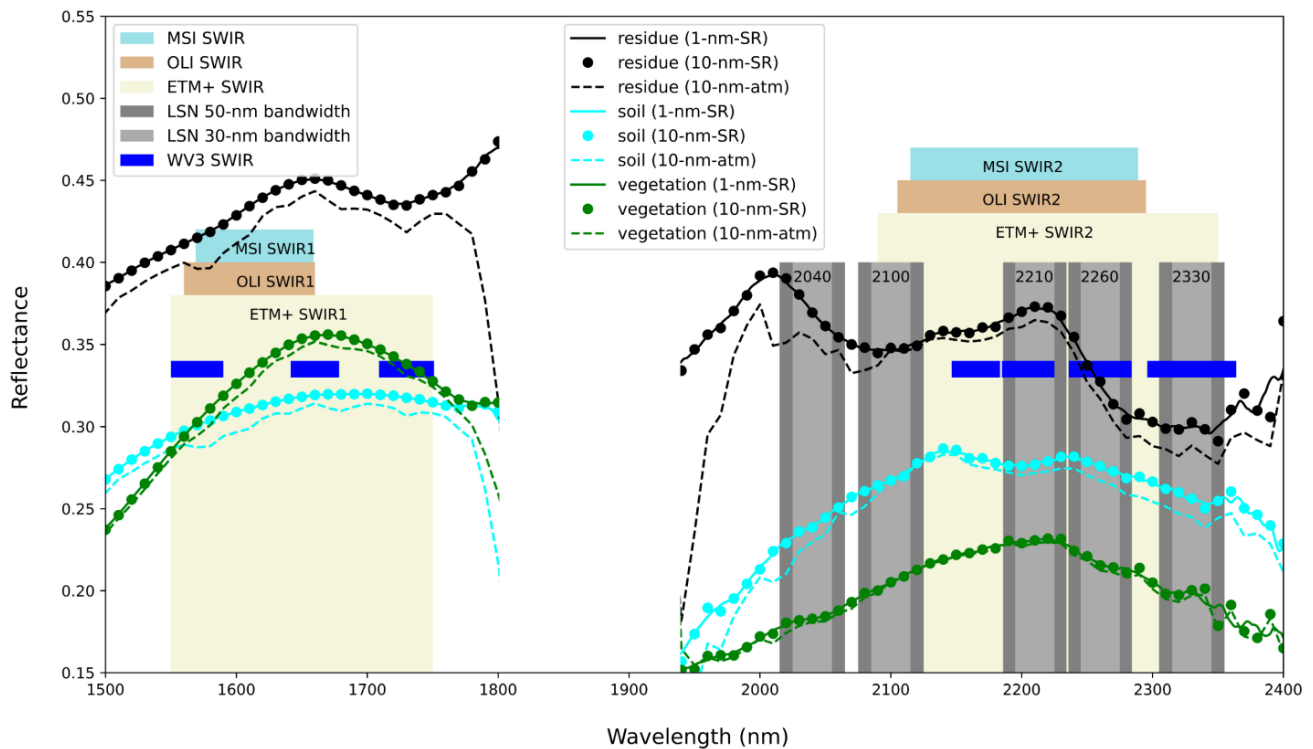

Figure 1. Comparison of SWIR bands on current multispectral sensors with field-collected spectra. The solid lines correspond to 1 nm interval (30 nm bandwidth) spectra, the points correspond to surface reflectance (SR)-processed 10 nm spectra, and dashed lines correspond to 10 nm spectra with atmospheric artifacts (atm-processed). The 10 nm spectra provide an illustration of imaging spectrometer capabilities, e.g., PRISMA and AVIRIS, with and without atmospheric correction. Previously evaluated Landsat Next (LSN) bands are depicted with gray bars [37]. For LSN bands, a combination of 2040, 2100, and 2210 nm bands corresponds to an absorption-centered index, e.g., CAI, and a combination of 2100, 2210, and 2260 nm corresponds to a peak-centered index, e.g., LCPCDI. Crop residue lignocellulose absorption features at 2100 and 2300 nm are effectively identified by LSN bands, and WV3 bands for the 2300 nm feature. Current Landsat/Sentinel-2 SWIR bands do not accurately resolve these absorption features.

2. Materials and Methods

To optimize the placement of Landsat Next SWIR bands for f_R estimation we used a database of agricultural field spectra from Dennison et al. (2019) [39]. The Dennison et al. (2019) dataset contains spectra that were originally collected by Daughtry and Hunt (2008) [30] and Quemada and Daughtry (2016) [40] at the United States Department of Agriculture Beltsville Agricultural Research Center (BARC) in Beltsville, MD, USA. Spectra were collected using Analytical Spectral Devices (ASD) field spectrometers (Malvern Panalytical, Westborough, MA, USA). Native sampling intervals of these field instruments is approximately 2 nm in the SWIR2 region, with a coarser spectral resolution of up to 12 nm depending on the specific instrument [39]. The instruments use cubic spline interpolation to resample spectra at a 1 nm interval.

Daughtry and Hunt (2008) collected 600 field spectra *in situ* from seven different BARC agricultural fields, and included varying cover of crop residue, soil, and three live crops (corn (*Zea mays* L.), soybeans (*Glycine max* (L.) Merr.), and wheat (*Triticum aestivum* L.)).

Quemada and Daughtry (2016) collected field spectra over manually manipulated plots with varying crop residue cover and surface moisture. For both datasets, spectra were collected using an 18° foreoptic positioned 2.3 m above the surface with a 0° view zenith angle. A digital camera was positioned next to the foreoptic, and a photograph was taken of the field-of-view of each spectrum. f_R, f_S, and f_{GV} were determined for each spectrum by point sampling the corresponding photograph (Daughtry and Hunt, 2008; Quemada and Daughtry, 2016). Quemada and Daughtry (2016) also measured soil and crop residue relative water content (RWC) for each field-of-view, and a RWC threshold of 60% used by Dennison et al. (2019) provided a total of 316 field spectra from this experiment. More details on RWC categories are provided in Section 2.4.

To assess f_R estimation performance, we applied an iterative wavelength shift approach to these agricultural spectra, hereafter referred to as the "BARC dataset" or simply "dataset", computing generalized spectral indices, then using linear regressions to model index values as a function of field-measured f_R. We performed the iterative wavelength shift analysis on two version of the BARC dataset: (1) 10 nm interval and bandwidth spectra with Gaussian spectral response functions previously published in Dennison et al. (2019), hereafter referred to as the "10 nm dataset" and (2) 1 nm interval, 30 nm bandwidth spectra calculated by applying a 30 nm moving-average filter to the original 1 nm field spectra collected by Daughtry and Hunt (2008) and Quemada and Daughtry (2016), hereafter referred to as the "1 nm interval dataset". The 10 nm dataset was processed to both surface reflectance (SR-processed) and surface reflectance with simulated sensor noise and atmospheric artifacts added (atm-processed). The atm-processed 10 nm spectra provide a general indication of atmospheric errors for Landsat Next f_R estimation since these errors were simulated for an imaging spectrometer with 10 nm bandwidths while Landsat Next will be a multispectral imaging system with ≥30 nm bandwidth for SWIR2 bands. Readers are directed to Dennison et al. (2019) [39] for a more thorough description of formulation of the 10 nm datasets. The 1 nm interval dataset was only processed to surface reflectance.

For both the 10 nm and 1 nm interval datasets, we created a subset of the datasets based on each spectrum's NDVI values, as abundant green vegetation has been found to impact f_R estimates. We computed NDVI from Landsat 8-simulated bands (Equation (1)) and selected the spectra with NDVI < 0.3 to represent low-vegetation conditions, producing 650 spectra for the 10 nm dataset and 643 spectra for the 1 nm interval dataset, with the difference in NDVI < 0.3 counts attributed to slight differences in band formation. The NDVI threshold of 0.3 was selected as this has been found to consistently represent a threshold for minimal green vegetation [20,31,34]. This allowed us to assess green vegetation effects by comparing results from the full-NDVI and NDVI < 0.3 datasets. The NDVI formula used in this study is shown in Equation (1).

$$\mathrm{NDVI} = (\mathrm{OLI}_5 - \mathrm{OLI}_4)/(\mathrm{OLI}_5 + \mathrm{OLI}_4) \tag{1}$$

where OLI denotes reflectance simulated for Landsat 8 OLI bands 4 and 5 (visible red and near infrared) as subscripts.

For the iterative wavelength shift analysis, we implemented an approach similar to Serbin et al. (2009b) [41], in which a two-band iterative generalized normalized difference index (gNDI) routine was used to determine which two reflectance wavelengths produced maximum correlation with ground-measured f_R. The Serbin et al. (2009b) gNDI approach was applied to several field spectroscopy studies conducted across the United States and results were aggregated to produce a composite R^2 value across sites. The original gNDI analysis was performed for all wavelengths from 400 nm to 2500 nm. In this study, we limited the iterative wavelength shift analysis to wavelengths between 2000 and 2350 nm as this portion of the SWIR region has been found to most consistently contain spectral variability related to the presence of lignocellulose absorption features present in NPV [38,41,42]. We excluded wavelengths greater than 2350 nm that contained significant sensor noise. To assess f_R estimation performance using the iterative wavelength shift approach, we computed the coefficient of determination (R^2) and root mean squared error

(*RMSE*) (Equations (2) and (3)) across all unique wavelength combinations between 2000 and 2350 nm by computing a spectral index and using ordinary least squares regression to model f_R.

$$R^2 = 1 - \frac{\sum_{i=1}^{n} (y_i - \hat{y}_i)^2}{\sum_{i=1}^{n} (y_i - \overline{y}_i)^2} \tag{2}$$

$$RMSE = \sqrt{\sum_{i=1}^{n} \frac{(\hat{y}_i - y_i)^2}{n}} \tag{3}$$

where y_i and $\hat{y}_i$ are observed (field-measured f_R) and predicted (index-estimated f_R) values, respectively, $\overline{y}_i$ is the average observed value, and n is the number of samples.

We performed the iterative wavelength shift analysis for generalized two-band indices (Equations (4) and (5)) and generalized three-band indices (Equations (11)–(13)). In performing this analysis across the 2000–2350 nm wavelength range, we seek to identify the wavelengths most useful for f_R characterization with Landsat Next SWIR bands. R^2 and *RMSE* are given equal consideration in performance assessments as maximizing explained variance and minimizing predictive error are both critical in selecting optimal wavelengths.

2.1. Two-Band Iterative Wavelength Shift Approach

The mathematical form of the gNDI spectral index from Serbin et al. (2009b) [4] is shown in Equation (4).

$$\text{gNDI}_{i,j,s} = \frac{R_{i,s} - R_{j,s}}{R_{i,s} + R_{j,s}} \tag{4}$$

where R denotes reflectance, subscripts i and j denote wavelengths for bands 1 and 2 and subscript s denotes a given spectrum. Each spectrum corresponds to a field-measured f_R value. The entire dataset of gNDI values was used to model f_R values (n = 916 for full-NDVI; n = 650/643 for NDVI < 0.3), resulting in an R^2 and *RMSE* value for each i, j wavelength in a two-dimensional spectral space.

In addition to implementing the two-band iterative gNDI approach, we also used a two-band generalized difference index (gDI) (Equation (5)), as Hively et al. (2021) [37] found this form of SWIR spectral index to be less susceptible to influence from green vegetation when estimating f_R.

$$\text{gDI}_{i,j,s} = R_{i,s} - R_{j,s} \tag{5}$$

Two established crop residue indices that provide examples of two-band normalized difference and simple difference index forms are the Shortwave Infrared Normalized Difference Residue Index (SINDRI) and Shortwave Infrared Difference Residue Index (SIDRI) [37,41] (Equations (6) and (7)). Note gNDI and gDI will evaluate all specific wavelength combinations in the 2000–2350 range, including combinations identical to SINDRI and SIDRI.

$$\text{SINDRI} = (R_{2210} - R_{2260}) / (R_{2210} + R_{2260}) \tag{6}$$

$$\text{SIDRI} = R_{2210} - R_{2260} \tag{7}$$

where R denotes reflectance, and the corresponding subscript denotes central wavelength for either a narrow band multispectral or hyperspectral sampling.

2.2. Three-Band Iterative Wavelength Shift Approach

We built on the two-band iterative wavelength shift approach from Serbin et al. (2009b) by including a third band. This modification was motivated by the fact that numerous studies have found three-band spectral indices to perform especially well for crop residue characterization and often better than two-band spectral indices [30,31,43,44]. We initially calculated two broad classes of indices using three-band generalized iterative approaches.

These classes included three-band absorption-at-center indices, hereafter referred to as side peak indices, and three-band peak-at-center indices, hereafter referred to as center peak indices. The "peak" terms refer to a higher reflectance value in regions spectrally adjacent to absorption features in dry plant matter centered near 2100 and 2300 nm (Figure 1). A well-established three-band side peak index is the Cellulose Absorption Index (CAI) [43] (Equation (8)). A more recently established, yet illustrative example of a three-band center peak index is the Lignin Cellulose Peak Center Difference Index (LCPCDI) [37] (Equation (9)). In this effort, we also test a second version of the LCPCDI with slightly shifted wavelengths (Equation (10)).

$$\text{CAI} = 0.5 * (R_{2040} + R_{2210}) - R_{2100} \tag{8}$$

$$\text{LCPCDI} = (2 * R_{2210}) - (R_{2100} + R_{2260}) \tag{9}$$

$$\text{LCPCDIv2} = (2 * R_{2220}) - (R_{2130} + R_{2270}) \tag{10}$$

In the case of CAI, the spectral "side" terms R_{2040} and R_{2210} generally exhibit higher reflectance values than the subtracted spectral "center" term R_{2100}, with this later term corresponding to a lignocellulose absorption feature around 2100 nm for an NPV target [38,42]. In the case of LCPCDI, the spectral center term R_{2210} generally exhibits higher reflectance than the R_{2100} and R_{2260} terms which overlap with lignocellulose absorption features at 2100 nm and 2300 nm, respectively, for an NPV target [38,42]. Figure 1 provides an illustration of these differences for example crop residue, soil, and green vegetation spectra from the BARC dataset. The 2040–2210 nm region/bands correspond to CAI with reflectance side peaks, while the 2100–2260 nm region/bands correspond to LCPCDI with a reflectance center peak for crop residue.

With the CAI and LCPCDI providing examples of side peak and center peak difference indices, respectively, we proceed noting that mathematically, side peak difference and center peak difference indices produce identical absolute values when computed with the same reflectance values for each band. Thus, for simplicity's sake, figures and references will proceed with mention of the generalized Center Peak Difference Index (gCPDI) only (Equation (11)). In addition to the gCPDI, we also computed a generalized Center Peak Ratio Index (gCPRI) (Equation (12)) to compare three-band ratio indices to the more commonly implemented three-band difference indices, e.g., CAI and LCPCDI. Unlike the side peak and center peak difference indices, the ratio versions of these indices will not produce identical absolute values and thus, a generalized Side Peak Ratio Index (gSPRI) is computed and shown in Equation (13) to illustrate this is a unique index compared to gCPRI.

$$\text{gCPDI}_{i,j,k,s} = (2 * R_{j,s}) - (R_{i,s} + R_{k,s}) \tag{11}$$

$$\text{gCPRI}_{i,j,k,s} = \frac{2 * R_{j,s}}{R_{i,s} + R_{k,s}} \tag{12}$$

$$\text{gSPRI}_{i,j,k,s} = \frac{R_{i,s} + R_{k,s}}{2 * R_{j,s}} \tag{13}$$

where *R* denotes reflectance, subscripts *i*, *j*, and *k* denote wavelengths for bands 1, 2, and 3, respectively. The subscript *s* denotes a given spectrum.

2.3. Iterative Wavelength Shift Approach Applied to BARC Spectra Datasets

We used the iterative wavelength shift approach to first analyze the 10 nm dataset processed with and without combined sensor noise and atmospheric artifacts (atm- and SR-processed, respectively). Leading with the 10 nm dataset wavelength shift analysis enabled us to determine whether atmospheric correction-based error sources, i.e., errors from atmospheric artifacts, were minimal enough to proceed with the wavelength shift analysis on the 1 nm interval dataset with surface reflectance processing only. While the atm-processed version of the 10 nm dataset only provided a limited comparison from one

simulation of errors from a standard atmosphere and specific sensor, the comparison to the SR-processed dataset is assumed to be generally informative. After the 10 nm dataset analysis was performed and results demonstrated minimal differences between the atm- and SR-processed datasets (Results Sections 3.1 and 3.3), we proceeded to apply the iterative wavelength shift approach to the 1 nm interval dataset (Results Sections 3.2 and 3.4).

We created an additional modified version of the three-band iterative wavelength shift approach applied to the 1 nm interval dataset to better identify multiple spectral regions useful for f_R estimation. While the results from the two-band wavelength shift analysis identified a single high performance (high R^2, low *RMSE*) spectral region for f_R estimation, the three-band analysis indicated the presence of multiple high R^2/low *RMSE* clusters, hereafter referred to as "high correlation clusters". To allow for the analysis of multiple high correlation clusters, we applied an empirical threshold of 2100 nm to band 1 to capture R^2 and *RMSE* for the slightly lower-correlation clusters. In the proceeding analyses, the terms "gCPDI", "gCPRI", and "gSPRI" denote the best performing bands across the entire 2000–2350 nm range, while "gCPDI$_{>2100}$", "gCPRI$_{>2100}$", and "gSPRI$_{>2100}$" denote best performing bands with a band 1 > 2100 nm constraint.

2.4. Assessment of Moisture and Green Vegetation Impacts on Crop Residue Estimation

The Quemada and Daughtry (2016) [40] subset of the 1 nm interval BARC dataset was used for assessment of the impact of soil and crop residue RWC on f_R estimation for top-performing wavelength shift analysis identified wavelengths. This dataset was originally collected by Quemada and Daughtry (2016) as part of a study assessing spectral index-based f_R estimation performance under varying RWC conditions. The total spectra (n = 316) were split into three RWC categories: 0.0–0.1 (n = 135), 0.1–0.25 (n = 101), and 0.25–0.60 (n = 77) [40]. These RWC classes were selected based on findings that crop residue spectral index performance was notably diminished after RWC exceeded 0.25. Quemada and Daughtry (2016) spectra contained no f_{GV}, meaning this dataset provides a largely controlled assessment of f_R estimation with f_S being the other cover type. We first assessed performance of the top-performing two- and three-band indices identified in the wavelength shift analysis (Equations (4), (5) and (11)–(13)) as a function of varying RWC using R^2 and *RMSE* metrics. We then compared the performance of iterative wavelength shift indices to established crop residue indices.

In addition to established CAI, SINDRI, and LCPCDI, we evaluated several additional indices tested in Hively et al. (2021) [37] including the Lignin-Cellulose Absorption Index (LCA), ratio version of CAI left peak (rCAI$_{LP}$), ratio version of CAI right peak (rCAI$_{RP}$), and the aforementioned heritage NDTI (Equations (14)–(17)).

$$LCA = ((2 * (R_{2210})) - (R_{2100} + R_{2330}) \tag{14}$$

$$rCAI_{LP} = (R_{2040} - R_{2100})/(R_{2040} + R_{2100}) \tag{15}$$

$$rCAI_{RP} = (R_{2210} - R_{2100})/(R_{2100} + R_{2210}) \tag{16}$$

$$NDTI = (OLI_6 - OLI_7)/(OLI_6 + OLI_7) \tag{17}$$

where R denotes reflectance, and the corresponding subscript denotes central wavelength for either a narrow band multispectral or hyperspectral sampling, and OLI denotes simulated reflectance from Landsat 8 OLI bands 6 and 7 (SWIR1 at 1610 nm and SWIR2 at 2200 nm, respectively) as subscripts.

Similar to the RWC analysis, the green vegetation analysis assessed the influence of varying f_{GV} levels on f_R estimation accuracy. For the green vegetation analysis, we used the Daughtry and Hunt (2008) [30] subset of the 1 nm interval BARC dataset which contained all original spectra published in that study (n = 600). Like the RWC analysis, spectra were split into f_{GV} classes of 0.0–0.1 (n = 327), 0.1–0.3 (n = 136), 0.3–0.6 (n = 46), 0.6–0.9 (n = 44), and 0.9–1.0 (n = 47). These class ranges were chosen to keep a similar number of samples for the higher f_{GV} ranges where the total samples were fewer relative to the lower f_{GV}

ranges. Like the RWC assessment, established crop residue indices were compared to top-performing iterative wavelength shift-identified indices and band wavelengths.

For our final analysis, we combined the RWC and green vegetation analyses to determine if the relative f_R estimation of the top-performing bands changed under these combined conditions. We computed a composite R^2 and *RMSE* for three RWC classes (0.0–0.6) and three f_{GV} classes (0.0–0.6) to determine the best-performing bands for Landsat Next SWIR2 as these composites equally weight performance across a range of conditions expected to diminish f_R estimation accuracy. These composite metric values were then compared to results from the 1 nm and 10 nm iterative wavelength shift analyses from the whole BARC dataset which skewed towards low f_{GV} and low RWC conditions. Our final analysis identified top-performing band centers and established wavelength tolerances by identifying the top-performing wavelength ranges for each band.

3. Results

The following sections proceed with findings from the two-band iterative wavelength shift analysis, hereafter referred to as "wavelength shift analysis" for brevity, first applied to the 10 nm BARC dataset (Section 3.1) followed by application to the 1 nm interval BARC dataset (Section 3.2). This analysis is followed by the three-band wavelength shift analysis applied to the 10 nm and 1 nm interval BARC datasets, respectively (Sections 3.3 and 3.4). In both two-band analyses, the maximum correlations in two-dimensional spectral space are visualized with black or gray circles while established indices are identified with red triangles for comparison. In the three-band analyses, histogram-style bars are used to identify maximum correlations in three-dimensional spectral space in addition to established indices with bars of different colors. In the wavelength shift analyses, use of the terms "band 1", "band 2", and "band 3" refers to bands comprising a given index where band 1 is the shortest wavelength and band 3 is the longest wavelength. The three-band wavelength shift analysis with the 1 nm interval BARC dataset features an additional routine assessing secondary spectral regions of high f_R estimation performance with the "band 1 > 2100 nm" constraint. The findings of the best performing wavelengths from the two-band and three-band wavelength shift analyses applied to the 1 nm interval dataset were then used to assess f_R estimation accuracy under conditions of variable RWC and green vegetation (Section 3.5).

3.1. Two-Band Wavelength Shift Analysis Using the 10 nm BARC Dataset

The two-band wavelength shift analysis applied to the 10 nm dataset demonstrated that wavelengths of highest f_R estimation performance cluster around SINDRI/SIDRI wavelengths of 2210 nm for band 1 and 2260 nm for band 2 as indicated by higher R^2 and lower *RMSE* (Figures 2 and 3). Figures 2 and 3 provide a side-to-side comparison of f_R estimation performance for gNDI and gDI indices. In nearly all cases, the SR- and atm-processed spectra showed minimal differences in performance with regards to difference in R^2 and *RMSE* and identified the same top-performing bands (Table 1 and Supplementary Materials).

While the atm-processed and SR-processed spectra produced similar results, f_R estimation performance varied more substantially between index type (gNDI vs. gDI), and NDVI level (minimal green vegetation vs. full range). Most notable were the large differences in R^2 values for the NDVI < 0.3 vs. full-NDVI datasets, with the former exhibiting R^2 values 0.25 greater for gNDI, and 0.07 greater for gDI, demonstrating the effect of spectral interference from green vegetation. For the full-NDVI dataset, gNDI maximum R^2 was 0.5303 while gDI was 0.6887 indicating that indices based on a simple difference may be more effective for f_R estimation under high levels of green vegetation. The maximum R^2 for gDI for the full-NDVI dataset occurred at wavelengths of 2220 nm and 2270 nm. The gNDI for the NDVI < 0.3 dataset produced the highest R^2 of all assessments (Figure 2a) with a value of 0.7879 for the same 2220 nm and 2270 nm wavelength combination, indicating these are ideal wavelengths for a two-band configuration for Landsat Next SWIR2. The f_R estima-

tion performance between gNDI and SINDRI was comparable ($R^2 = 0.7879$ vs. $R^2 = 0.7766$, $RMSE = 0.1408$ vs. $RMSE = 0.1587$, respectively). In the comparable gDI analysis with the NDVI < 0.3 dataset, the top-performing band 1 was 2210 nm, while the top-performing band 2 was 2330 nm. While this represents a rather large wavelength shift for band 2 when compared to SIDRI with 2210 and 2260 nm bands, the f_R estimation results were similar between gDI and SIDRI ($R^2 = 0.7578$ vs. $R^2 = 0.7306$, $RMSE = 0.1504$ vs. $RMSE = 0.1587$). Figure 2b illustrates that while 2330 nm was top performing as band 2, a wide range of shorter band 2 wavelengths offer comparatively high f_R estimation accuracy. These results are summarized in Table 1.
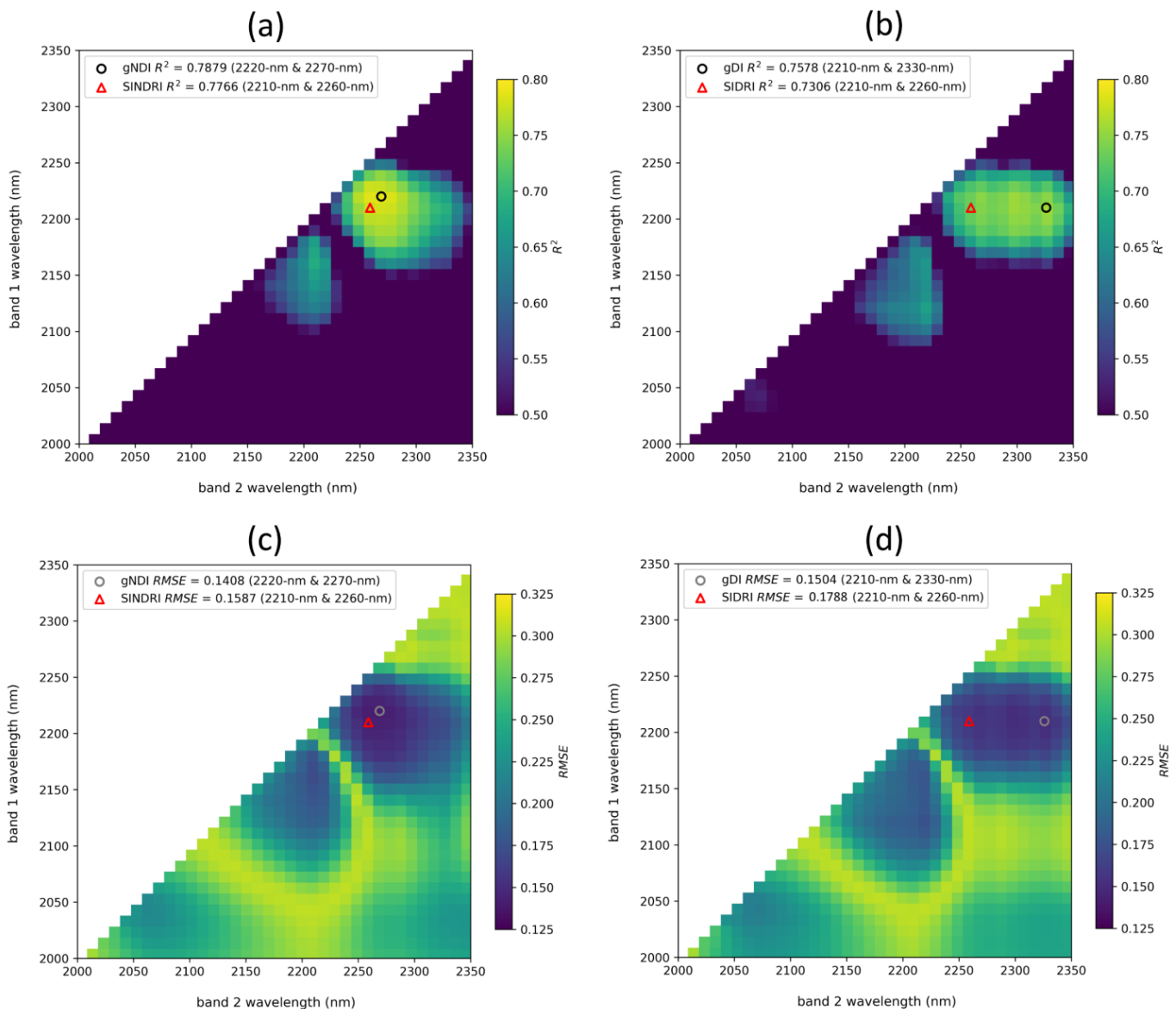

Figure 2. Performance metrics for two-band wavelength shift indices computed from the 10 nm dataset NDVI < 0.3 subset with n = 650: (**a**) gNDI-R^2, (**b**) gDI-R^2, (**c**) gNDI-*RMSE*, (**d**) gDI-*RMSE*. In all panels, the gray/black circles represent the band combination that produced the best f_R estimation performance, as defined by the respective performance metric. The red triangles depict the band combination of a comparable heritage index. Results shown are from SR-processed spectra. The results for atm-processed spectra identified the same top-performing bands as the SR-processed spectra and are shown in Table 1. Supplementary Materials Figures S1 and S2 provide side-by-side comparisons of SR-processed (panels a and c) and atm-spectra (panels b and d) results.

Figure 3. Performance metrics for two-band wavelength shift indices computed from the full-NDVI 10 nm dataset with n = 916: (**a**) gNDI-R^2, (**b**) gDI-R^2, (**c**) gNDI-*RMSE*, (**d**) gDI-*RMSE*. In all panels, the gray/black circles represent the band combination that produced the best f_R estimation performance, as defined by the respective performance metric. The red triangles depict the band combination of a comparable heritage index. Results shown are from SR-processed spectra. The results for atm-processed spectra identified the same top-performing bands as the SR-processed spectra and are shown in Table 1. Supplementary Materials Figures S3 and S4 provide side-by-side comparisons of SR-processed (panels a and c) and atm-spectra (panels b and d) results.
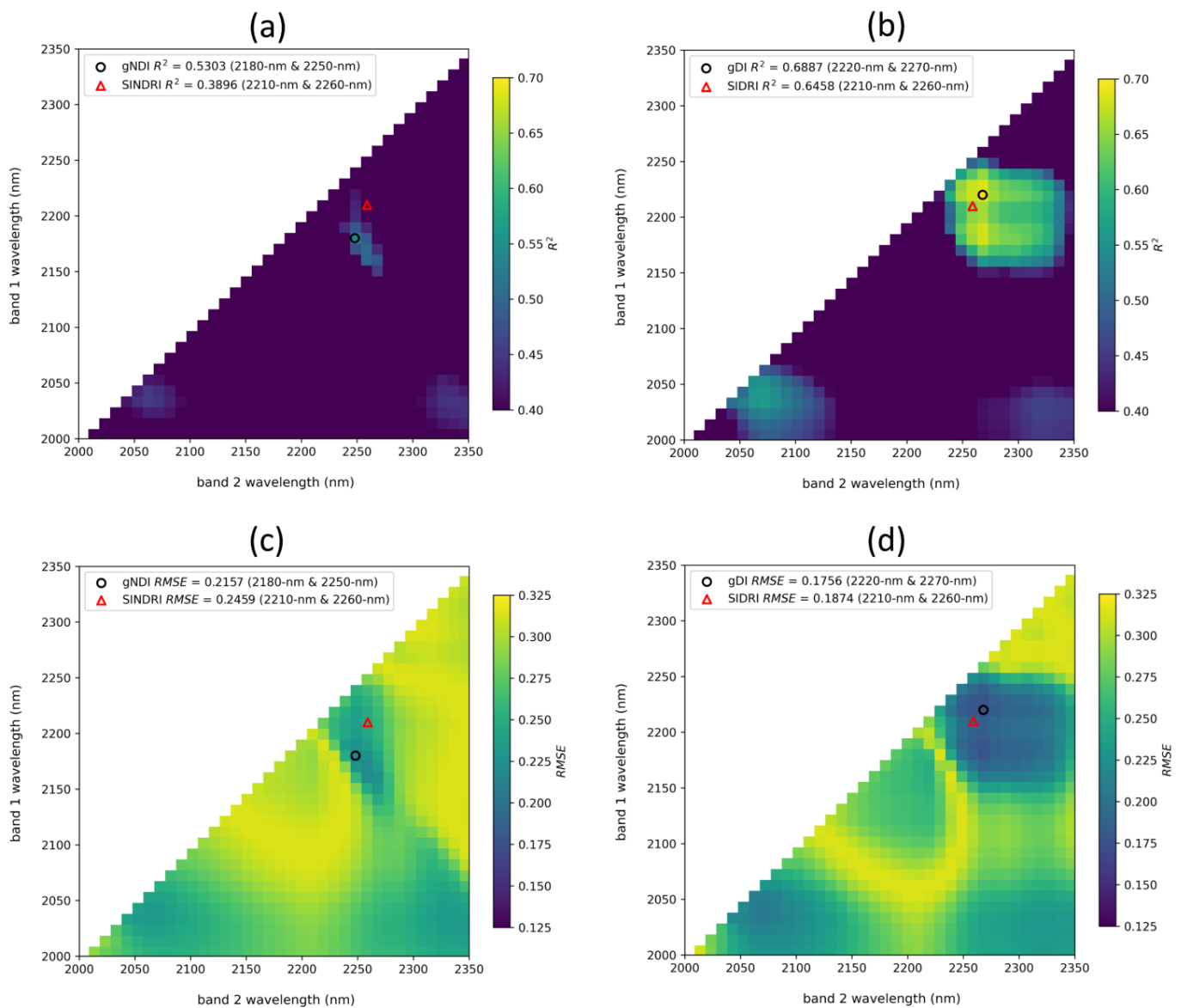
3.2. Two-Band Wavelength Shift Analysis Using the 1 nm Interval BARC Dataset

Given that the comparison between SR- and atm-processed 10 nm spectra exhibited minimal differences in performance compared to other analysis factors, we proceeded with an assessment with the 1 nm interval SR dataset to increase the spectral precision of our analysis. We approached the 1 nm interval wavelength shift analysis in a nearly identical manner as the 10 nm analysis noting that the SR-processed 10 nm spectra and 1 nm interval spectra are similar in processing, but not identical in terms of band properties, as the 1 nm interval dataset features a 30 nm band width expected for a multispectral imaging system on Landsat Next, while the 10 nm spectra correspond to those of an imaging spectrometer.

Table 1. 10 nm BARC dataset f_R estimation performance comparison with the two-band wavelength shift analysis. The highest R^2 values for NDVI < 0.3 (upper rows; n = 650) and full-NDVI (lower rows; n = 916) have been bolded. The lowest *RMSE* for NDVI < 0.3 and full-NDVI have been bolded. Band-1 and Band-2 denote the wavelengths with the highest f_R estimation performance for both R^2 and *RMSE*. For example, for gNDI, 2220 and 2270 nm exhibited the highest R^2 values, and these same wavelengths exhibited the lowest *RMSE*.

Index	NDVI	n	R^2	*RMSE*	Band-1	Band-2
gNDI-SR	<0.3	650	**0.7879**	**0.1408**	**2220**	**2270**
gNDI-atm	<0.3	650	0.7734	0.1458	2220	2270
gDI-SR	<0.3	650	0.7578	0.1504	2210	2330
gDI-atm	<0.3	650	0.7428	0.1553	2210	2330
SINDRI-SR	<0.3	650	0.7766	0.1587	2210	2260
SINDRI-atm	<0.3	650	0.7610	0.1653	2210	2260
SIDRI-SR	<0.3	650	0.7306	0.1788	2210	2260
SIDRI-atm	<0.3	650	0.7089	0.1783	2210	2260
gNDI-SR	full	916	0.5303	0.2157	2180	2250
gNDI-atm	full	916	0.4709	0.2290	2180	2250
gDI-SR	full	916	**0.6887**	**0.1756**	**2220**	**2270**
gDI-atm	full	916	0.6870	0.1761	2220	2270
SINDRI-SR	full	916	0.3896	0.2459	2210	2260
SINDRI-atm	full	916	0.3613	0.2516	2210	2260
SIDRI-SR	full	916	0.6458	0.1874	2210	2260
SIDRI-atm	full	916	0.6505	0.1861	2210	2260

For both the 1 nm interval and 10 nm datasets, gNDI and gDI performed quite similarly. Both datasets demonstrated that gNDI produced higher maximum R^2 values and lower minimum *RMSE* values than gDI. Overall, the 1 nm interval dataset wavelength shift analysis (summarized in Table 2) exhibited higher performance than the 10 nm dataset analysis summarized in Table 1. This is likely attributable to a higher resolution interval sampling, although the band width (30 nm vs. 10 nm) and spectral response function (boxcar vs. Gaussian) likely played a role as well. Isolating the contributions of these specific band parameters was not an objective of this research effort, but it is notable that the 1 nm interval bands were configured in a manner more closely simulating the expected band configurations for Landsat Next as currently established [2]. Despite the differences in band configurations, similar optimal wavelengths were established in 1 nm interval and 10 nm analyses. The 1 nm interval gNDI exhibited the highest performance in f_R estimation with band 1 at 2226 nm and band 2 at 2263 nm, although SINDRI was quite comparable in terms of performance (R^2 = 0.8222 vs. R^2 = 0.8145, *RMSE* = 0.1296 vs. *RMSE* = 0.1324, respectively). For the 1 nm interval gDI analysis, band placements were similar to the 10 nm analysis with band 1 at 2211 nm, and a slightly different band 2 placement at 2316 nm. Figure 4 provides a side-by-side comparison of 1 nm gNDI and gDI performance (NDVI < 0.3) and demonstrates general patterns nearly identical to the 10 nm analysis. The same is true for Figure 5 providing a comparison of gNDI and gDI under the full-NDVI range, where gDI with band 1 at 2227 nm and band 2 at 2259 nm exhibited much higher performance in f_R estimation than the best performing gNDI (gDI R^2 = 0.7258 vs. gNDI R^2 = 0.5865). Overall, the two-band 1 nm interval results indicate that band 1 placement can be shifted up to 2230 nm (2210–2230 nm), and the results largely agree with 10 nm analysis that optimal placement for band 2 is between 2260 and 2270 nm in a case of Landsat Next SWIR2 being comprised of two bands.

Table 2. Two-band wavelength shift analysis performance for 1 nm interval (30 nm bandwidth) BARC dataset. For nearly all statistical performance metrics (R^2, *RMSE*), the 1 nm interval dataset results demonstrate higher explained variance and lower error than the 10 nm dataset in f_R estimation but identify very similar top-performing bands (see Table 1). Band-1 and Band-2 denote the wavelengths with the highest f_R estimation performance for both R^2 and *RMSE*. Top-performing bands and indices for each NDVI case have been bolded.

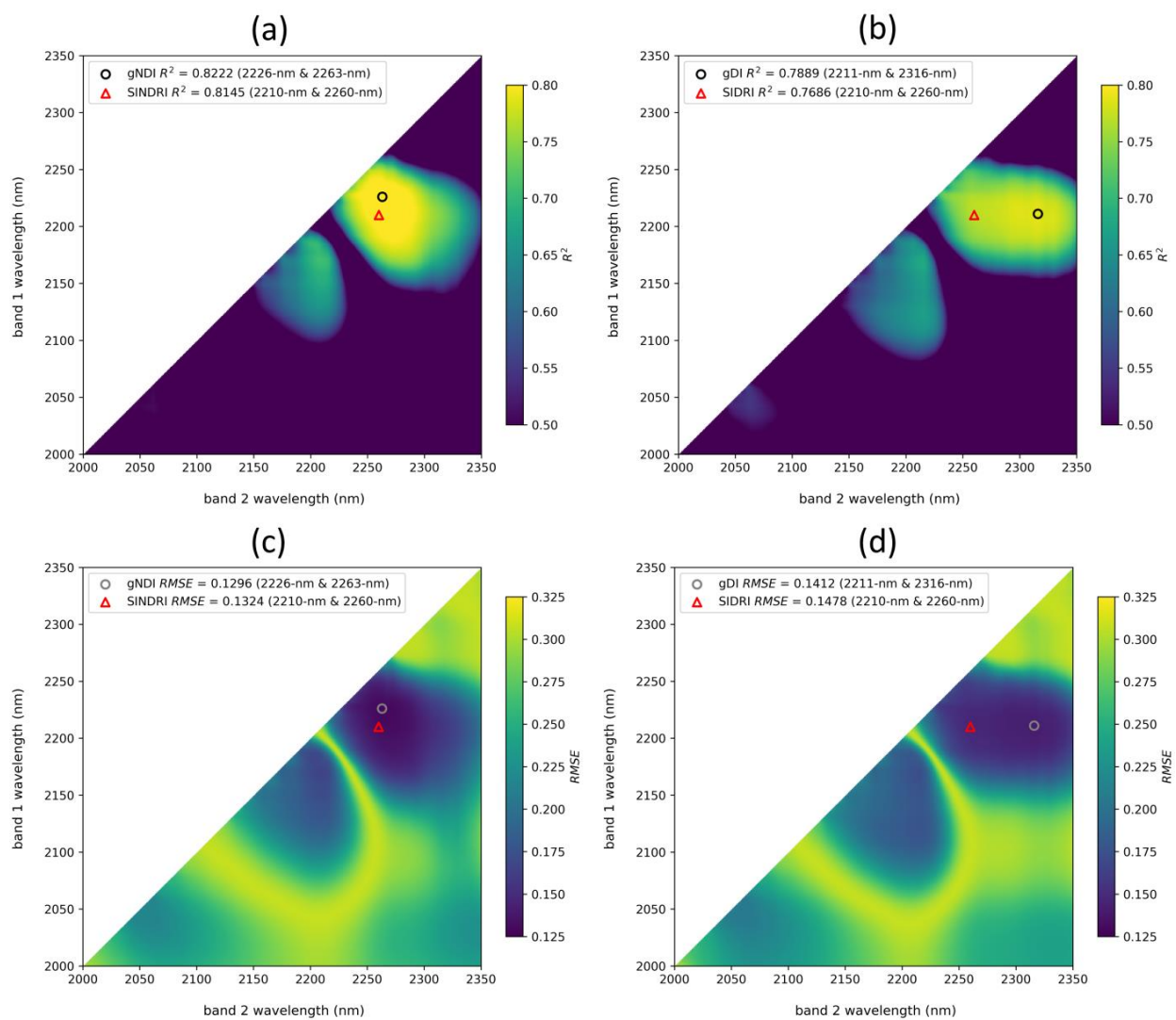| Index	NDVI	n	R^2	*RMSE*	Band-1	Band-2
gNDI	<0.3	643	**0.8222**	**0.1296**	**2226**	**2263**
gDI	<0.3	643	0.7889	0.1412	2211	2316
SINDRI	<0.3	643	0.8145	0.1324	2210	2260
SIDRI	<0.3	643	0.7686	0.1478	2210	2260
gNDI	full	916	0.5865	0.2024	2170	2256
gDI	full	916	**0.7258**	**0.1648**	**2227**	**2259**
SINDRI	full	916	0.4144	0.2409	2210	2260
SIDRI	full	916	0.7022	0.1718	2210	2260

Figure 4. Performance metrics for two-band gNDI and gDI using 1 nm interval dataset with NDVI < 0.3 subset with n = 643: (**a**) gNDI-R^2, (**b**) gDI-R^2, (**c**) gNDI-*RMSE*, (**d**) gDI-*RMSE*. All spectra processed to surface reflectance. In all panels, the gray/black circles represent the band combination that produced the best f_R estimation performance, as defined by the respective performance metric. The red triangles depict the band combination of a comparable heritage index.

Figure 5. Performance metrics for two-band gNDI and gDI using 1 nm interval full-NDVI dataset with n = 916: (**a**) gNDI-R^2, (**b**) gDI-R^2, (**c**) gNDI-*RMSE*, (**d**) gDI-*RMSE*. All spectra were processed to surface reflectance. In all panels, the black circles represent the band combination that produced the best f_R estimation performance, as defined by the respective performance metric. The red triangles depict the band combination of a comparable heritage index.
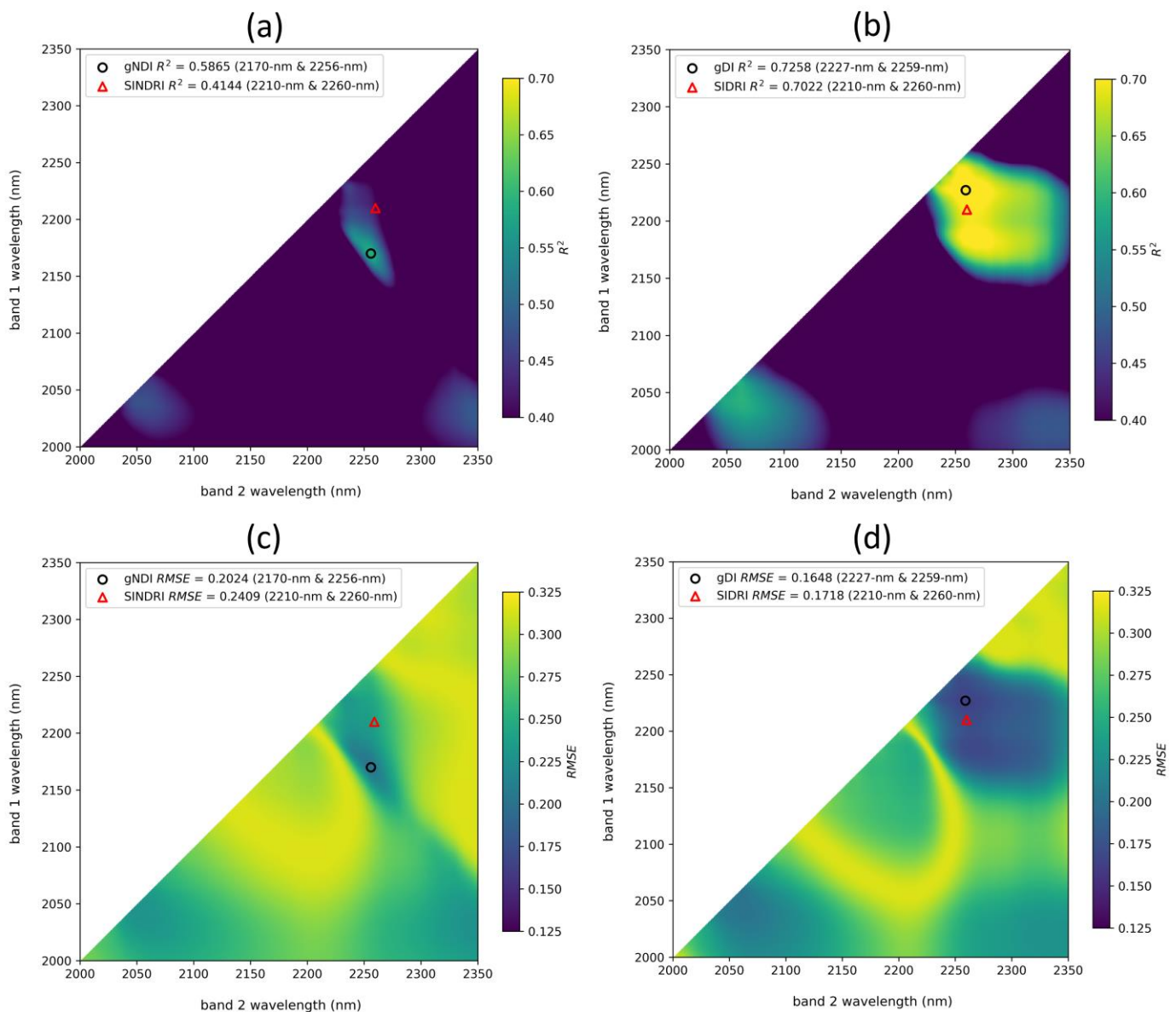
3.3. Three-Band Wavelength Shift Analysis Using the 10 nm BARC Dataset

For the three-band wavelength shift analysis applied to the 10 nm dataset, the CAI-type bands were top performers (Figures 6 and 7). For the NDVI < 0.3 datasets, the best performing three-band index was gCPRI-SR with 2030 nm, 2080 nm, and 2220 nm band centers ($R^2 = 0.8148$ and *RMSE* = 0.1315). For the full-NDVI dataset, the best performing three-band index was gSPRI-SR with 2030, 2110, and 2210 nm band centers, ($R^2 = 0.7176$ and *RMSE* = 0.1673). In no case did the top-performing bands change between the SR- and atm-processed datasets, although SR-processed datasets performed better.

Despite the high performance of CAI-type bands, LCPCDIv2 performed better than CAI itself for f_R estimation with the NDVI < 0.3 dataset (Table 3). However, LCPCDIv2 and LCPCDI exhibited a much lower performance in f_R estimation than CAI for the full-NDVI dataset. The top-performing difference-based index (comparable formulation to CAI and

LCPCDI) was gCPDI-SR with wavelengths of 2050, 2090, and 2220 nm. However, the gCPDI-SR exhibited a lower f_R estimation performance (R^2 = 0.7822 and *RMSE* = 0.1427) compared to gCPRI-SR indicating ratio-based indices may perform better than difference-based indices overall, even with very similar top-performing wavelengths (Figure 6).
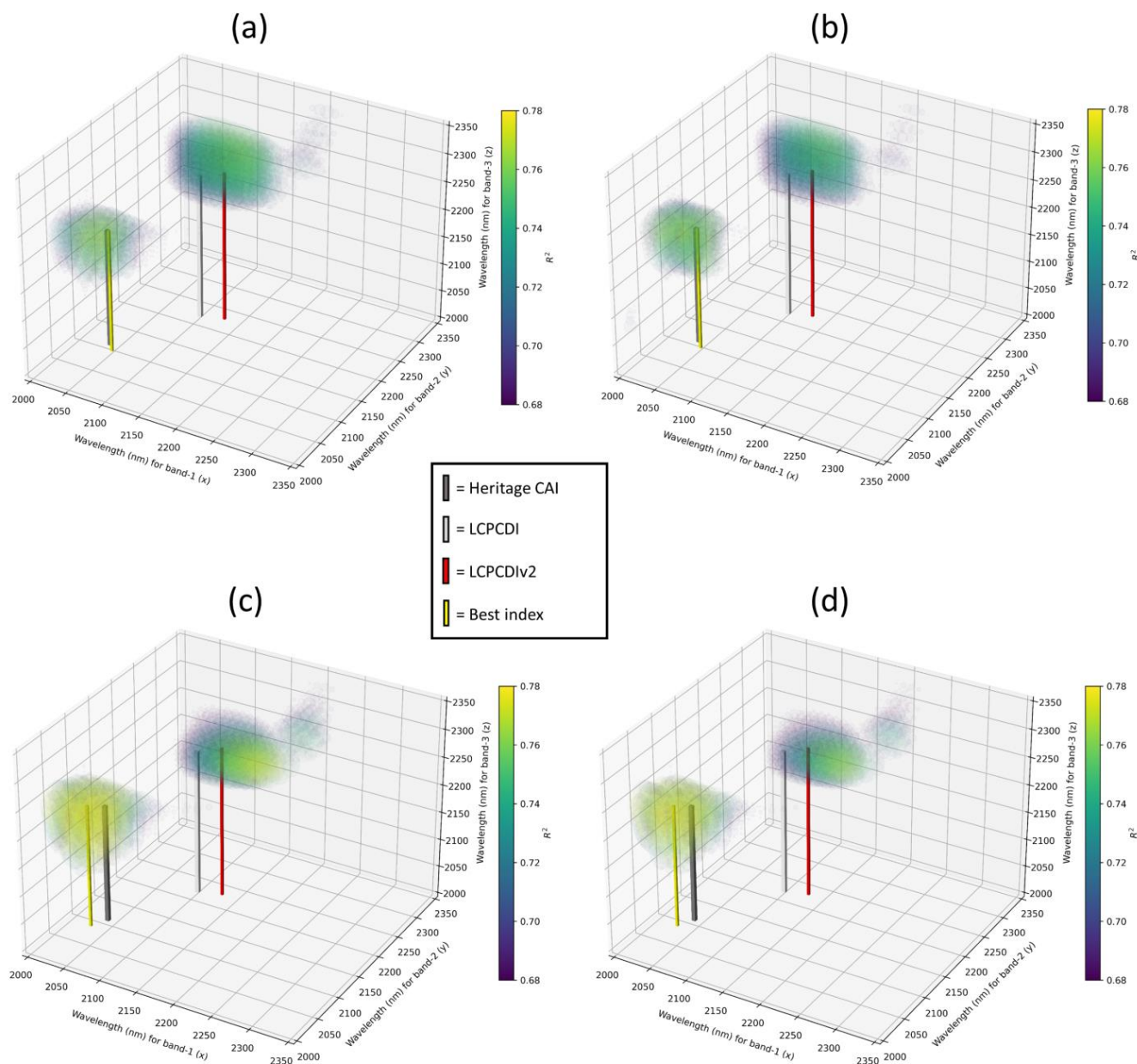

Figure 6. Three-band wavelength shift analysis f_R estimation results for the 10 nm dataset with NDVI < 0.3 subset. (**a**) gCPDI (NDVI < 0.3) surface reflectance, (**b**) gCPDI (NDVI < 0.3) with atmospheric artifacts, (**c**) gCPRI (NDVI < 0.3) surface reflectance, (**d**) gCPRI (NDVI < 0.3) with atmospheric artifacts. Note that in the case of panels a–b, the maximum correlation band combination is so similar to CAI band locations that the yellow bar partially obscures the dark gray bar. The spectral location of LCPCDIv2 (with band 1 central wavelength of 2130 nm) relative to LCPCDI shifts closer to a secondary high correlation cluster. NDVI < 0.3 dataset has n = 650. Rotational, interactive versions of panels a and c are provided in Supplementary Materials Figures S5 and S6.

Combined impacts of high NDVI values and atmospheric artifacts reduced f_R estimation performance in the full-range NDVI dataset. Figure 7 shows a pronounced decrease

in the area of the high correlation cluster for gCPDI-atm (panel b) compared to gCPDI-SR (panel a), specifically in the CAI wavelength region. This decrease in performance occurs along band 3 (the z-axis) primarily. This level of performance decrease was not visible in Figure 6 with the NDVI < 0.3 dataset nor is a performance decrease present for the ratio indices (Figure 7, panels c–d). The full-NDVI gCPDI-SR and gCPDI-atm have similar maximum R^2 values of 0.6941 and 0.6830, respectively (Table 3). Full-NDVI CAI-SR also exhibits a comparable R^2 value of 0.6716. However, for the full-NDVI CAI-atm, R^2 value drops to 0.5807. This is the largest atmospheric artifact-based decrease in f_R estimation performance for a single index in the entire iterative wavelength shift analysis (Results Sections 3.1–3.4). This finding potentially indicates that CAI-type difference indices may not be as robust to green vegetation interference when atmospheric artifacts—water vapor and carbon dioxide residuals in this case—are also present. However, under these conditions, ratio-based indices with CAI-type wavelengths performed well and exhibited the only well-defined high correlation clusters in panels c and d for Figure 7.

Table 3. Three-band wavelength shift analysis comparison for 10 nm BARC dataset. The highest R^2 values for NDVI < 0.3 (upper rows) and full-NDVI (lower rows) have been bolded. In nearly all cases, spectral bands close to CAI-type bands (2040, 2100, 2210 nm) are top performers. NDVI < 0.3 dataset has n = 650. Full-NDVI dataset has n = 916. Band-1, Band-2, and Band-3 denote the wavelengths with the highest f_R estimation performance for both R^2 and *RMSE*.

Index	NDVI	n	R^2	*RMSE*	Band-1	Band-2	Band-3
gCPDI-SR	<0.3	650	0.7822	0.1427	2050	2090	2220
gCPDI-atm	<0.3	650	0.7816	0.1431	2050	2090	2220
gSPDI-SR	<0.3	650	0.7822	0.1427	2050	2090	2220
gSPDI-atm	<0.3	650	0.7816	0.1431	2050	2090	2220
gCPRI-SR	<0.3	650	**0.8148**	**0.1315**	**2030**	**2080**	**2220**
gCPRI-atm	<0.3	650	0.8082	0.1341	2030	2080	2220
gSPRI-SR	<0.3	650	0.8121	0.1325	2030	2080	2220
gSPRI-atm	<0.3	650	0.8026	0.1361	2030	2080	2220
CAI-SR	<0.3	650	0.7486	0.1533	2040	2100	2210
CAI-atm	<0.3	650	0.7507	0.1529	2040	2100	2210
LCPCDI-SR	<0.3	650	0.7129	0.1638	2100	2210	2260
LCPCDI-atm	<0.3	650	0.6947	0.1692	2100	2210	2260
LCPCDIv2-SR	<0.3	650	0.7625	0.1490	2130	2220	2270
LCPCDIv2-atm	<0.3	650	0.7516	0.1527	2130	2220	2270
gCPDI-SR	full	916	0.6941	0.1741	2040	2090	2160
gCPDI-atm	full	916	0.6830	0.1772	2030	2080	2160
gSPDI-SR	full	916	0.6941	0.1741	2040	2090	2160
gSPDI-atm	full	916	0.6830	0.1772	2030	2080	2160
gCPRI-SR	full	916	0.7148	0.1681	2030	2110	2210
gCPRI-atm	full	916	0.7143	0.1682	2030	2110	2210
gSPRI-SR	full	916	**0.7176**	**0.1673**	**2030**	**2110**	**2210**
gSPRI-atm	full	916	0.7171	0.1674	2030	2110	2210
CAI-SR	full	916	0.6716	0.1804	2040	2100	2210
CAI-atm	full	916	0.5807	0.2038	2040	2100	2210
LCPCDI-SR	full	916	0.4622	0.2308	2100	2210	2260
LCPCDI-atm	full	916	0.4381	0.2360	2100	2210	2260
LCPCDIv2-SR	full	916	0.5782	0.2044	2130	2220	2270
LCPCDIv2-atm	full	916	0.5564	0.2097	2130	2220	2270

3.4. Three-Band Wavelength Shift Analysis Using the 1 nm Interval BARC Dataset

We applied the three-band wavelength shift analysis to the 1 nm interval dataset, including a sub-processing routine identifying the differences in performance between the spectral locations of the top-performing wavelength shift indices across the 2000–2350 nm range (approximately corresponding to CAI band spectral region; ~2000–2200 nm) and

spectral regions where the band 1 > 2100 nm constraint was imposed (approximately corresponding to LCPCDI spectral region; ~2100–2300 nm).
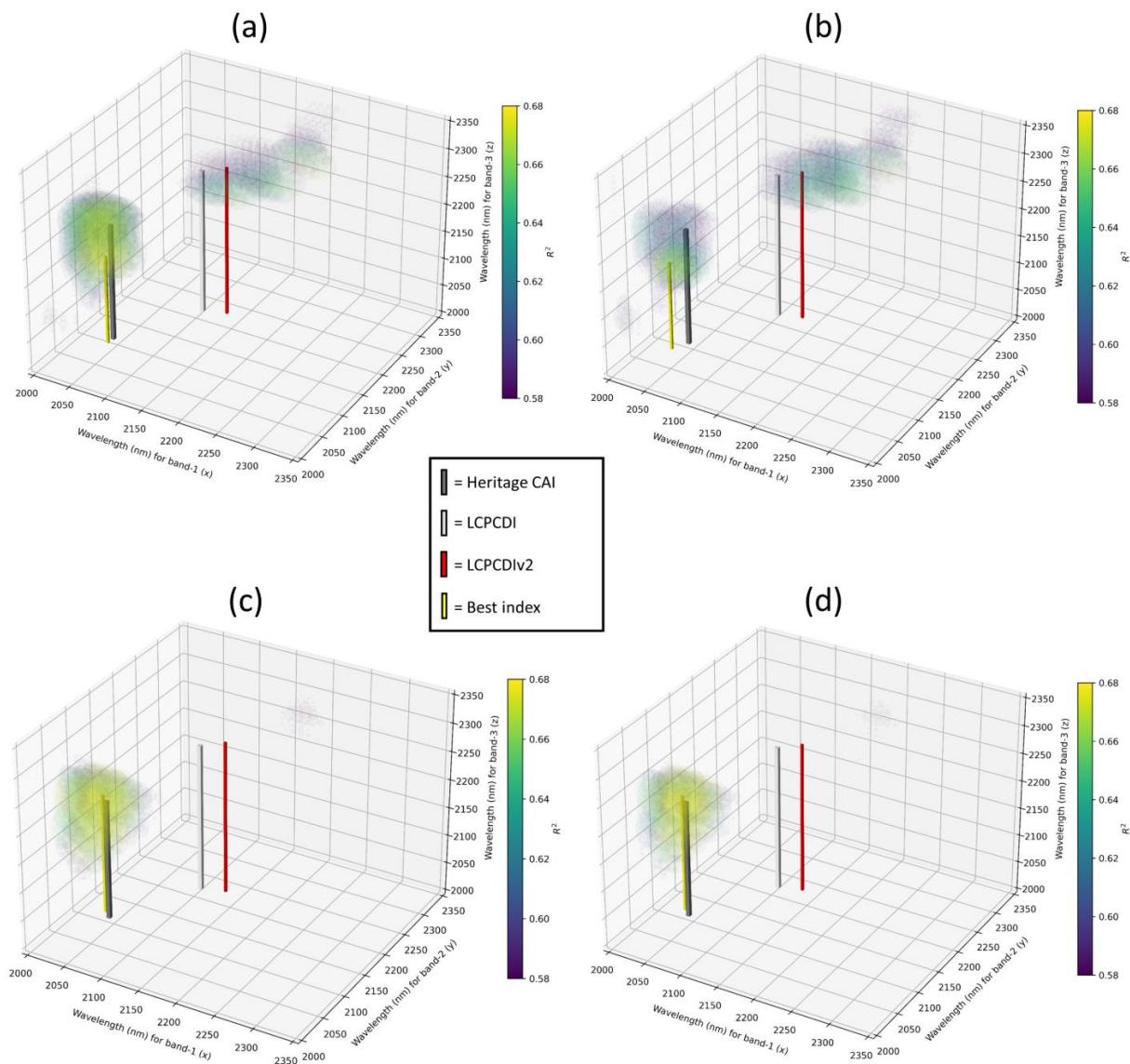

Figure 7. Three-band wavelength shift analysis f_R estimation results with the 10 nm full-NDVI dataset. (**a**) gCPDI (full-NDVI) surface reflectance, (**b**) gCPDI (full-NDVI) with atmospheric artifacts, (**c**) gCPRI (full-NDVI) surface reflectance, (**d**) gCPRI (full-NDVI) with atmospheric artifacts. Note that the top-performing index wavelengths (determined by R^2) largely cluster in the CAI wavelength region. Although the LCPCDI high correlation clusters were maintained for the difference indices (panels a–b), this was not so for the ratio indices (panels c–d). Full-NDVI dataset has n = 916. Rotational, interactive versions of panels a and c are provided in Supplementary Materials Figures S7 and S8.

The findings of the three-band wavelength shift analysis indicate that bands with CAI-type wavelengths are top performers. For the NDVI < 0.3 dataset the gCPRI was the top-performing index with wavelength positions of 2031, 2085, and 2216 nm (Figure 8, Table 4). These top-performing bands are similar to CAI bands of 2040, 2100, and 2210 nm. The top-performing gCPRI$_{>2100}$ shifted to a three-band combination of 2184, 2216, and 2262 nm. The differences in R^2 between gCPRI vs. gCPRI$_{>2100}$ were not substantial for the NDVI < 0.3 dataset, with 0.8397 compared to 0.8262, respectively. When the gCPRI$_{>2100}$ was evaluated with the full-NDVI dataset, the best performing bands were 2223, 2225, and 2258 nm. This indicates that having a third band provided little additional utility in

f_R estimation performance compared to a two-band difference index with a wavelength range limited to 2000–2350 nm. This is directly evidenced by comparing the three-band gCPRI$_{>2100}$ R^2 of 0.7260 to the two-band gDI R^2 of 0.7258 (2227 nm and 2259 nm bands) for the full-NDVI dataset. An important limitation to address with this analysis and associated findings is that the longer wavelength cutoff of 2350 nm did not allow for evaluation of three-band indices fully resolving a 2300 nm absorption feature as this would ideally include noise-free reflectance observations extending to 2400 nm for the third band.
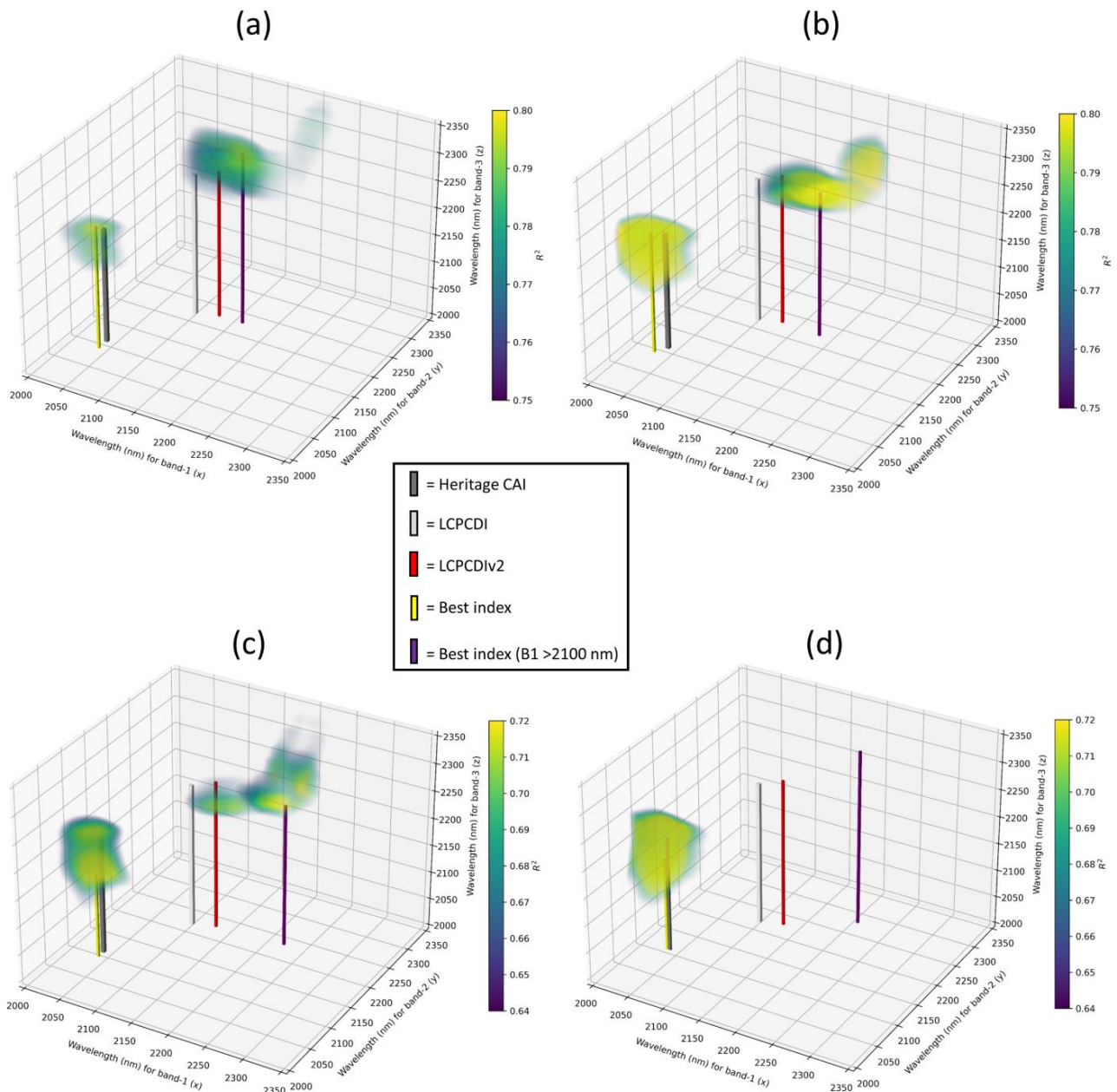

Figure 8. Three-band wavelength shift analysis f_R estimation results with the 1 nm interval dataset. (**a**) gCPDI (NDVI < 0.3), (**b**) gCPRI (NDVI < 0.3), (**c**) gCPDI (full-NDVI), (**d**) gCPRI (full-NDVI). Note that in all cases the maximum correlation cluster (yellow bar) is again close to CAI (dark gray bar). While LCPCDIv2 performs well in panels a–c, the best index with the band 1 (B1) > 2100 nm constraint generally shifts the best performing band 1 closer to 2180 nm. Panel d with the full-NDVI and gCPRI is the only case where the LCPCDI-type correlation cluster is not visible as R^2 values do not exceed 0.64.

Table 4. Three-band wavelength shift analysis for 1 nm interval BARC dataset. The rows with bold text indicate the top-performing indices in f_R estimation with and without the band 1 > 2100 nm constraint and the NDVI < 0.3 and full-NDVI datasets. The underlined values indicate top performance with the band 1 < 2100 nm constraint. Band-1, Band-2, and Band-3 denote the wavelengths with the highest f_R estimation performance for both R^2 and *RMSE*, with the only exception to this being gCRPI where R^2 top-performing Band-1 wavelength was 2031 nm, while *RMSE* top-performing Band-1 wavelength was 2032 nm (2031* denotes this exception).

Index	NDVI	n	R^2	*RMSE*	Band-1	Band-2	Band-3
gCPDI	<0.3	643	0.8021	0.1367	2041	2083	2225
gSPDI	<0.3	643	0.8021	0.1367	2041	2083	2225
gCPRI	<0.3	643	**0.8397**	**0.1231**	**2031***	**2085**	**2216**
gSPRI	<0.3	643	0.8360	0.1244	2031	2084	2216
gCPDI$_{>2100}$	<0.3	643	0.8009	0.1371	2163	2220	2313
gSPDI$_{>2100}$	<0.3	643	0.8009	0.1371	2163	2220	2313
gCPRI$_{>2100}$	<0.3	643	<u>0.8262</u>	<u>0.1281</u>	<u>2184</u>	<u>2216</u>	<u>2262</u>
gSPRI$_{>2100}$	<0.3	643	0.8241	0.1289	2185	2216	2262
CAI	<0.3	643	0.7714	0.1469	2040	2100	2210
LCPCDI	<0.3	643	0.7466	0.1547	2100	2210	2260
LCPCDIv2	<0.3	643	0.7806	0.1440	2130	2220	2270
gCPDI	full	916	0.7338	0.1624	2041	2089	2154
gSPDI	full	916	0.7338	0.1624	2041	2089	2154
gCPRI	full	916	0.7567	0.1553	2036	2100	2169
gSPRI	full	916	**0.7581**	**0.1548**	**2036**	**2111**	**2217**
gCPDI$_{>2100}$	full	916	<u>0.7260</u>	<u>0.1648</u>	<u>2223</u>	<u>2225</u>	<u>2258</u>
gSPDI$_{>2100}$	full	916	0.7260	0.1648	2223	2225	2258
gCPRI$_{>2100}$	full	916	0.6517	0.1858	2208	2270	2320
gSPRI$_{>2100}$	full	916	0.6574	0.1843	2208	2270	2320
CAI	full	916	0.7119	0.1690	2040	2100	2210
LCPCDI	full	916	0.4984	0.2229	2100	2210	2260
LCPCDIv2	full	916	0.5862	0.2025	2130	2220	2270

3.5. Moisture and Green Vegetation Impacts on Fractional Crop Residue (f_R) Cover Estimation

The broad band NDTI index, based on heritage SWIR1 and SWIR2 bands and commonly used in crop residue studies, performed worse than all other indices across RWC classes (Figure 9). Two-band CAI variants exhibited a pronounced performance drop (decrease in R^2 and increase in *RMSE*) for the higher RWC class (0.25 to 0.60). This is likely attributable to the fact that the 2040 nm band is sensitive to liquid water absorption, which changes the slope of reflectance in this portion of the SWIR2 spectrum. The 2100 nm band, with a 30 nm band width, likely has some sensitivity to water absorption as well. When high RWC is present, two-band index sensitivity to RWC may be greater than f_R when computed from 2040 and 2100 nm bands. In contrast, the three-band CAI appears to remain stable, likely because it estimates absorption feature depth and in theory should be less impacted by diminished reflectance in the 2040 nm band since the more stable 2200 nm band would help compensate for shorter wavelength changes in reflectance slope (Figure 10). In general, the three-band indices performed better than the two-band, but SINDRI maintained relatively high performance ($R^2 \sim 0.9$) and was least impacted by change in RWC class (Figure 10). Overall, index performance for the RWC analysis (Figure 10) was somewhat higher than for the overall analysis (Tables 1–4) likely due to the absence of green vegetation in the reduced dataset.

In the green vegetation analysis, nearly all indices exhibited a decrease in both R^2 and *RMSE* above 0.3 f_{GV}. For reference, an f_{GV} level of 0.3 has been found to correspond to an NDVI value of approximately 0.473 while an f_{GV} level of 0.6 corresponds to an NDVI of 0.683 for green cover crops [45]. The decrease in both R^2 and *RMSE* is likely attributed to variance in index values diminishing for a given f_{GV} category while also becoming less correlated with f_R (regression error and explained variance both decreasing). NDTI was

the worst performing index as indicated by low R^2 and increased *RMSE* compared to other indices (Figures 11 and 12). The two-band rCAI$_{RP}$ was the second worst performing index overall after NDTI. In terms of the heritage indices (Figure 11), three-band CAI was again a top-performing index. The wavelength shift index that performed best across a range of f_{GV} conditions was the gSPRI computed from the full-NDVI dataset (Section 3.4). The gCPDI (full-NDVI dataset) also performed well. Compared to these two top-performing wavelength shift indices, CAI was a comparable performer and performed far better than SINDRI for f_{GV} categories above 0.3. In the majority of cases for RWC and f_{GV} analyses, the top-performing index bands are spectrally close to CAI band wavelengths (Figures 9–12).
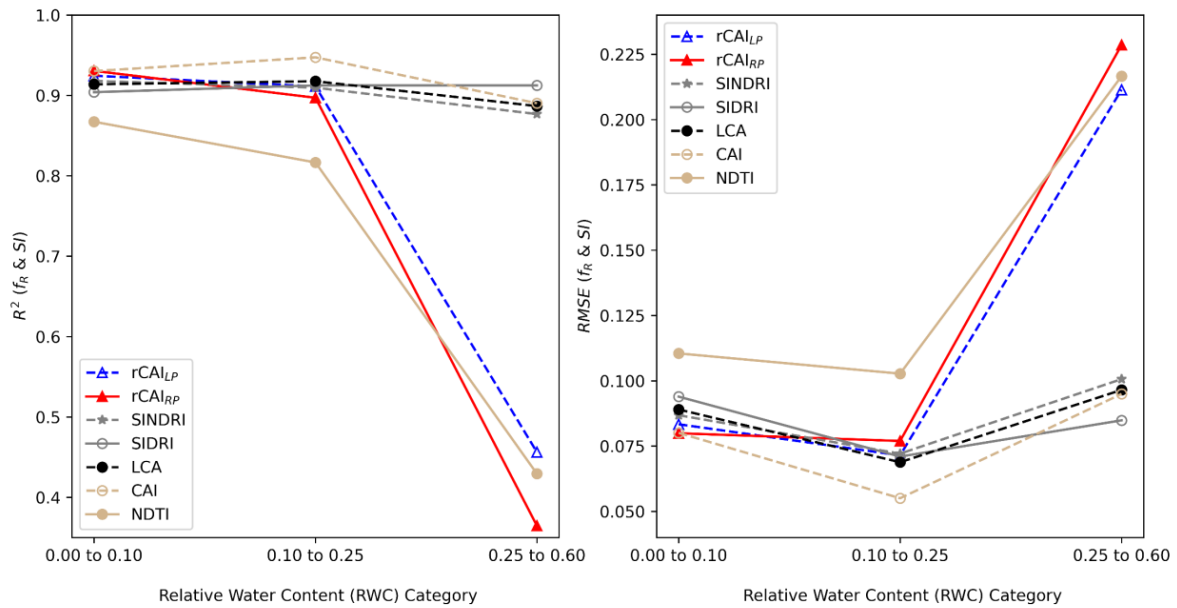

Figure 9. Heritage spectral index (SI) f_R estimation performance according to RWC class. Left panel is R^2 and right panel is *RMSE*.
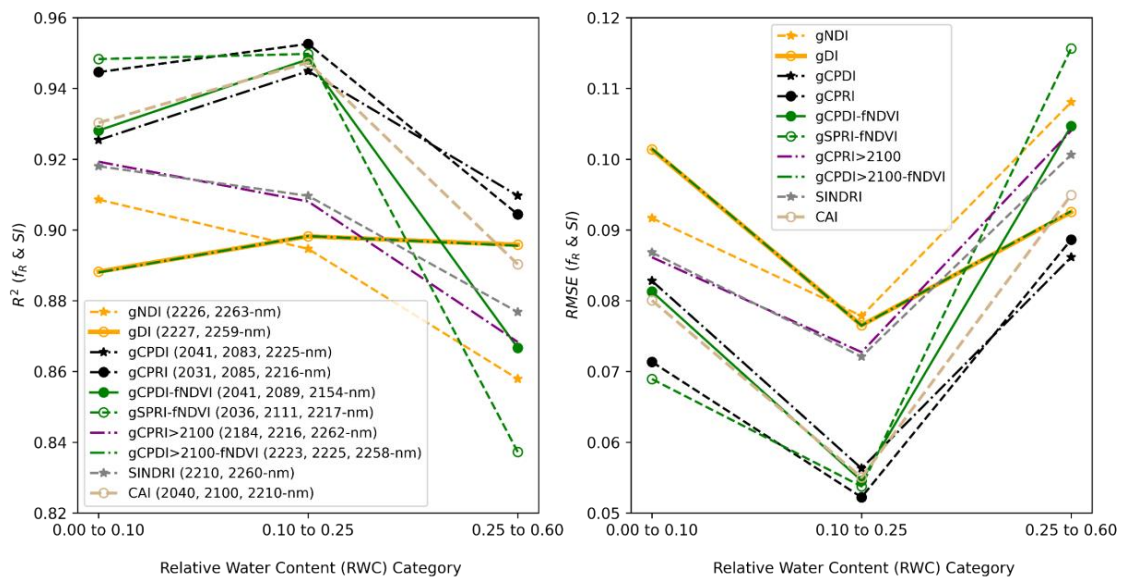

Figure 10. Wavelength shift spectral index (SI) f_R estimation performance according to RWC class (with heritage SINDRI and CAI for performance comparison). Left panel is R^2 and right panel is *RMSE*. Note that "-fNDVI" denotes wavelength shift index derived from the 1 nm interval full-NDVI dataset, other wavelength shift indices are derived from the NDVI < 0.3 dataset.
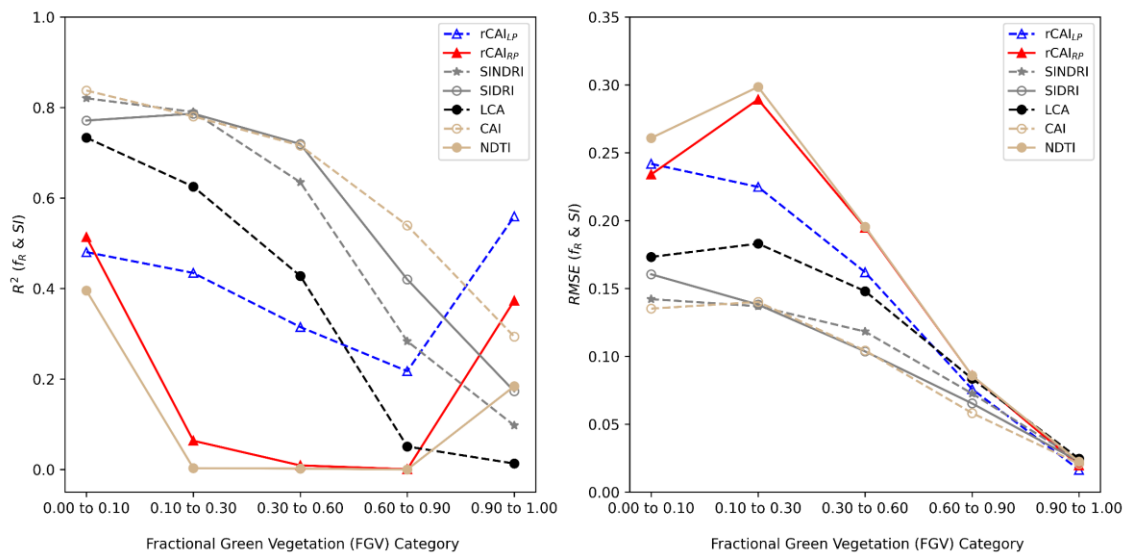
Figure 11. Heritage spectral index (SI) f_{GV} estimation performance according to f_{GV} (FGV) class. Left panel is R^2 and right panel is *RMSE*.
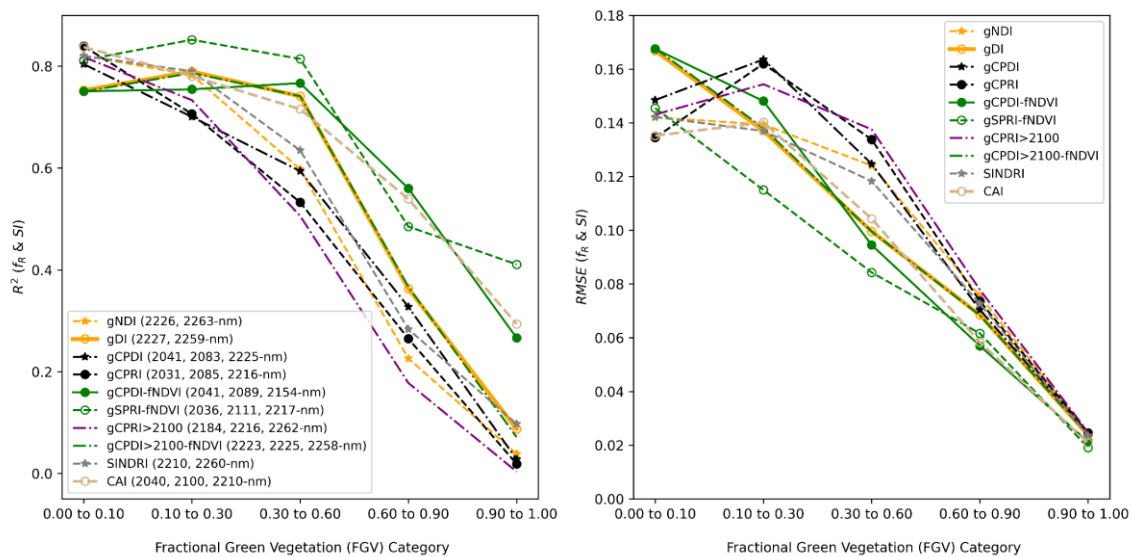

Figure 12. Wavelength shift spectral index (SI) f_{GV} estimation performance according to f_{GV} (FGV) class, with heritage SINDRI and CAI for performance comparison. Left panel is R^2 and right panel is *RMSE*.

The findings of the RWC and green vegetation analyses are summarized in Table 5. The last column of Table 5 is an average value for R^2 and *RMSE* computed across the three RWC classes and three f_{GV} classes up to 0.6. This f_{GV} cutoff was selected as it corresponds to an NDVI value approaching 0.7 where f_R retrievals would become increasingly challenging due to low fractional coverage and physical shading by standing green vegetation. For the two-band analysis, conventional SINDRI and SIDRI bands at 2210 and 2260 nm performed best in f_R estimation across the different classes (Table 5). However, in terms of the three-band analysis, the conventional CAI was outperformed by gSPRI-fNDVI with slightly different bands at 2036, 2111, and 2217 nm. We noted that in terms of *RMSE*, all top-performing indices were close in derivation to CAI, exhibiting only slight differences in wavelength. These wavelength differences provide insights as to what wavelength tolerances may be appropriate for a three-band Landsat Next SWIR2 configuration. We used these wavelength ranges to establish final central wavelengths.

Table 5. Comparison of f_R estimation results for each index by RWC and f_{GV} (GV) classes. The last column is an average computation of index performance across all RWC classes and the GV classes from 0.0 to 0.6 (* denotes higher f_{GV} classes were excluded from computation). The best performing *RMSE* (with associated R^2) are indicated by bold text (two 2-band indices and five 3-band indices). The central wavelengths and ranges for bands 1, 2, and 3 in the best performing three-band indices are used to establish final band locations.

Index	Metric	RWC-0.0-0.1	RWC-0.1-0.25	RWC-0.25-0.6	GV-0.0-0.1	GV-0.1-0.3	GV-0.3-0.6	GV-0.6-0.9	GV-0.9-1.0	Average *
NDTI	R^2	0.867	0.817	0.429	0.396	0.003	0.002	0.000	0.184	0.419
SINDRI	R^2	0.918	0.910	0.877	0.820	0.790	0.635	0.283	0.097	**0.825**
SIDRI	R^2	0.904	0.912	0.912	0.771	0.787	0.719	0.420	0.173	**0.834**
LCA	R^2	0.914	0.918	0.887	0.733	0.625	0.428	0.051	0.013	0.751
CAI	R^2	0.930	0.947	0.890	0.838	0.780	0.716	0.539	0.294	**0.850**
rCAI$_{LP}$	R^2	0.924	0.911	0.456	0.480	0.434	0.315	0.217	0.559	0.587
rCAI$_{RP}$	R^2	0.931	0.897	0.365	0.513	0.064	0.009	0.001	0.373	0.463
gCPDI	R^2	0.925	0.945	0.910	0.804	0.701	0.594	0.327	0.028	**0.813**
gCPRI	R^2	0.945	0.953	0.904	0.839	0.706	0.533	0.265	0.019	**0.813**
gCPDI-fNDVI	R^2	0.928	0.948	0.867	0.751	0.755	0.767	0.560	0.266	**0.836**
gSPRI-fNDVI	R^2	0.948	0.950	0.837	0.812	0.852	0.814	0.485	0.411	**0.869**
gCPRI$_{>2100}$	R^2	0.919	0.908	0.868	0.818	0.733	0.506	0.178	0.004	0.792
gCPDI$_{>2100}$	R^2	0.888	0.898	0.896	0.750	0.787	0.741	0.367	0.071	0.827
gNDI	R^2	0.909	0.895	0.858	0.821	0.783	0.598	0.226	0.038	0.810
gDI	R^2	0.888	0.898	0.896	0.753	0.790	0.741	0.363	0.087	0.828
NDTI	*RMSE*	0.110	0.103	0.217	0.261	0.299	0.196	0.086	0.022	0.197
SINDRI	*RMSE*	0.087	0.072	0.101	0.142	0.137	0.118	0.073	0.024	**0.109**
SIDRI	*RMSE*	0.094	0.071	0.085	0.160	0.138	0.104	0.065	0.023	**0.109**
LCA	*RMSE*	0.089	0.069	0.097	0.173	0.183	0.148	0.084	0.025	0.126
CAI	*RMSE*	0.080	0.055	0.095	0.135	0.140	0.104	0.058	0.021	**0.102**
rCAI$_{LP}$	*RMSE*	0.083	0.071	0.211	0.242	0.225	0.162	0.076	0.016	0.166
rCAI$_{RP}$	*RMSE*	0.080	0.077	0.229	0.234	0.289	0.195	0.086	0.020	0.184
gCPDI	*RMSE*	0.083	0.056	0.086	0.148	0.164	0.125	0.070	0.024	**0.110**
gCPRI	*RMSE*	0.071	0.052	0.089	0.134	0.162	0.134	0.074	0.025	**0.107**
gCPDI-fNDVI	*RMSE*	0.081	0.055	0.105	0.168	0.148	0.095	0.057	0.021	**0.108**
gSPRI-fNDVI	*RMSE*	0.069	0.054	0.116	0.145	0.115	0.084	0.062	0.019	**0.097**
gCPRI$_{>2100}$	*RMSE*	0.086	0.073	0.104	0.143	0.154	0.138	0.078	0.025	0.116
gCPDI$_{>2100}$	*RMSE*	0.101	0.077	0.093	0.168	0.138	0.100	0.068	0.024	0.113
gNDI	*RMSE*	0.092	0.078	0.108	0.142	0.139	0.124	0.076	0.024	0.114
gDI	*RMSE*	0.101	0.077	0.093	0.167	0.137	0.100	0.069	0.024	0.112

For the three-band analysis, top-performing band 1 wavelengths ranged from 2031 to 2041 nm for CAI, gCPDI, gCPRI, gCPDI-fNDVI, and gSPRI-fNDVI with the central band in this range being identical to band 1 of top-performing gSPRI-fNDVI. For this reason, placing band 1 at 2036 nm with a ±5 nm tolerance will likely perform best in f_R estimation. For band 2, wavelengths typically fell within the lignocellulose absorption feature centered at 2100 nm, but with a wide spectral range spanning from 2083 nm to 2111 nm for the top-performing indices. Given this finding, centering band 2 at 2097 nm with a ± 14 nm tolerance is expected to yield high f_R estimation performance. The range of band 3 wavelengths was quite large, spanning from 2154 to 2225 nm. The gCPDI-fNDVI band 3 wavelength of 2154 nm was somewhat of an outlier compared to other top-performing indices. Table 4 indicates that the 2150–2170 nm wavelength range for band 3 may be unique to center peak indices computed with the full-NDVI dataset. Comparatively, side-peak ratio indices performed better in f_R estimation for the full-NDVI dataset as shown in Table 4. Given these findings, we limited the wavelength range of band 3 to the three central wavelengths of the top five indices in Table 5, establishing a new range of 2210 to 2217 nm and a band 3 center of 2214 nm with a tolerance of ± 11 nm (ranging up to 2225 nm). This central wavelength and tolerance range would not include the 2150–2170 nm wavelengths for band 3 but does cover the conventional CAI band 3 at 2210 nm.

4. Discussion

To evaluate optimal Landsat Next SWIR band placements for f_R estimation, we applied wavelength shift analyses to the 1 nm interval (30 nm bandwidth) and 10 nm BARC spectra datasets and assessed f_R estimation accuracy. For the two-band wavelength shift analysis applied to the 10 nm dataset, wavelengths similar to the 2210 and 2260 nm bands that formulate the well-established SINDRI index outperformed other spectral regions in f_R

estimation. The f_R estimation accuracies of SINDRI with NDVI < 0.3 observed in this study fell between those previously established in Serbin et al. (2009b) [41] with an R^2 of 0.741 for a U.S.-scale dataset and Hively et al. (2018) [20] with an R^2 of 0.940 for a single-date, local-scale dataset. In the two-band wavelength shift analyses with gNDI, the top-performing bands were 2220 and 2270 nm with the NDVI < 0.3 dataset. When the two-band analyses were performed with the full-NDVI dataset, the 2220 and 2270 nm bands were again top-performing but with the gDI rather than gNDI.

For the 1 nm interval dataset analysis with NDVI < 0.3, gNDI was the top performer in f_R estimation with identified bands at 2226 and 2263 nm, but SINDRI offered very similar performance with f_R estimation differences less than 0.01 for R^2 and 0.0028 for *RMSE*. For the full-NDVI 1 nm interval dataset analysis, gDI was the best performing index where it exhibited considerably higher f_R estimation performance than gNDI even with gDI having similar top-performing bands at 2227 nm and 2259 nm. The findings of both two-band analyses (10 nm and 1 nm interval datasets) indicate that the approximate band ranges of 2210–2230 nm for band 1 and 2260–2270 nm for band 2 provide a best overall solution for the case of Landsat Next SWIR2 being comprised of two bands. While gDI maintained more consistent performance for the different NDVI thresholds than gNDI, gDI was not the top performer in f_R estimation and further would be expected to be the least stable of all generalized indices tested in both the two- and three-band analyses. The expected lack of stability compared to normalized difference indices is due to the gDI, including SIDRI, being reliant on a simple reflectance difference between two bands and featuring no-scaling type adjustments that may partially compensate for variation in surface brightness, including ground-shading, surface anisotropy/bidirectional reflectance distribution function effects, and uncertainties/errors in surface reflectance retrievals [46]. With the Landsat Next mission's global mapping focus, this presents a challenge, as f_R estimation accuracy would vary considerably depending on f_{GV} cover. While multiple indices (including NDVI) could be used for pixel-level f_R estimation using two SWIR bands at 2200 nm and 2270 nm, this approach could produce inconsistencies in derived f_R products, and complicates product development compared to a single index approach.

The inclusion of an additional band for the three-band wavelength shift analyses (Results Sections 3.2 and 3.4) improved f_R estimation performance while being less impacted by f_{GV} compared to the two-band indices in general. This finding comports with previous work by Serbin et al. (2009b) [41] who demonstrated that the three-band CAI exhibited similar f_R estimation performance to SINDRI across a wide range of conditions but was notably less impacted by the presence of green vegetation. For the three-band wavelength shift analysis applied to the 10 nm dataset, the spectral regions associated with CAI bands (2030–2050 nm, 2080–2110 nm, and 2210–2220 nm) were found to be top performers for the NDVI < 0.3 dataset (Figure 6) and the full-NDVI dataset (Figure 7), indicating robust performance across a range of vegetation conditions. Wang et al. (2013) [47] found CAI to be more correlated with vegetation dry matter content than both SINDRI and NDTI while also being less correlated with vegetation moisture content, partially explaining CAI's high f_R estimation accuracy in this study compared to other indices. This is a critical performance difference between the three-band and two-band indices since crop residue surveys are often conducted during the spring season when green winter cover crops have reached maximum biomass and summer cash crops are emerging, meaning that satellite-based f_R estimation techniques would require resilience to f_{GV} effects. For the 10 nm analysis, the gCPRI with 2030, 2080, and 2220 nm bands was found to be top performing in f_R estimation for the NDVI < 0.3 dataset. For the full-NDVI dataset, gSPRI with 2030, 2110, and 2210 nm bands was found to be top performing. Only the central band 2 shifted by more than 10 nm in this comparison. The overall findings presented in Table 3 indicate that for indices computed from CAI-type wavelengths (2040, 2100, and 2210 nm), there is a fair degree of latitude in spectral placement of band 2.

For the 1 nm interval dataset, gCPRI exhibited top performance with bands at 2031, 2085, and 2216 nm and an R^2 = 0.8397 and *RMSE* = 0.1231. This was the top f_R esti-

mation performance across all wavelength shift analyses (Results Sections 3.1–3.4), and these wavelengths are nearly identical to the top-performing bands in the 10 nm dataset analysis. Also comparable to the 10 nm dataset analysis, for the 1 nm interval analysis with full-NDVI gSPRI was top-performing with three bands at 2036, 2111, and 2217 nm and an $R^2 = 0.7581$ and *RMSE* = 0.1548. Compared to gSPRI, gCPRI performed quite comparably for the full-NDVI dataset in terms of f_R estimation performance while identifying the same band 1 wavelength of 2036 nm but identified different band 2 wavelengths (2100 nm vs. 2111 nm) and band 3 wavelengths (2169 nm vs. 2217 nm). This indicates that there is a fair degree of latitude in the placements of bands 2 and 3, while band 1 should ideally remain fairly fixed. Although CAI-type wavelengths were top-performing across the three-band wavelength shift analysis, ratio indices outperformed difference indices by R^2 values greater than 0.035 in certain cases. Further, difference indices were more prone to errors in estimation of f_R when both full-NDVI and atmospheric artifacts were present (Figure 7 panels a–b vs. panels c–d). Assessment of index type was not the primary focus of this study, but considering these findings, a more in-depth investigation of index formation could provide critical information on development of f_R products suitable for regional and global scale mapping efforts.

To provide a more thorough assessment of the wavelength shift analysis findings in determining final band recommendations for Landsat Next SWIR2, we evaluated top-performing indices under conditions of varying RWC and f_{GV}. Nearly all narrow band multispectral indices comprised of multiple SWIR2 bands resolving lignocellulose absorption features exhibited R^2 values approaching or exceeding 0.9. NDTI, comprised of a single SWIR2 band, was the only index that had R^2 values well below 0.9. Further, NDTI exhibited a greater rate of decrease in R^2 values as a function of increasing RWC than other indices, indicating this index proves unreliable in f_R estimation under conditions of varying moisture, as has been demonstrated by analyses in Quemada et al. (2018) and Quemada and Daughtry (2016) [32,40]. The NDTI-f_R correlations of $R^2 \sim 0.45$ for the 0.25–0.60 RWC class were slightly lower, but in a similar range as those observed across sites with multitemporal Landsat imagery in Thoma et al. (2004) [48]. Our findings indicate that RWC variability may partially explain lower performance in NDTI-based f_R estimation, as would be expected in analyses using multitemporal satellite imagery. Decreased f_R estimation performance of the high RWC class (0.25 to 0.6) was also observed for the two-band CAI type indices (Figure 9) as would be expected for two-band indices with wavelengths of varying liquid water absorption strength. Comparatively, the performance of two-band SIDRI and SINDRI indicate that indices with 2210 nm and 2260 nm bands provide far better performance in f_R estimation in terms of robustness to RWC in the event of Landsat Next being limited to two SWIR2 bands. In the two-band case, SINDRI/SIDRI bands at ~2210 nm and 2260 nm perform much better than other two-band combinations, e.g., two-band CAI variants. For the green vegetation analysis, both two-band CAI indices performed somewhat poorly at higher f_{GV} levels. LCA and SINDRI performed moderately and SIDRI somewhat better than SINDRI. CAI exceeded all established indices in f_R estimation with increasing f_{GV} (Figure 11).

In comparison to the wavelength shift generalized indices, (Figures 10 and 12), CAI still maintains good performance relative to the generalized indices, but gSPRI-fNDVI is also a top performer across vegetation classes and is the highest performer for the 0.10–0.30 and 0.30–0.60 categories. The gSPRI-fNDVI bands (2036, 2111, and 2217 nm) were top performing in the RWC analysis. In the three-band wavelength shift analysis with the 1 nm interval BARC dataset, the wavelengths of the best performing band 1 were between 2031 and 2041 nm, indicating that this narrow spectral range represents an ideal band placement. The central wavelength of this range is 2036 nm, which was the best performing band in the top performing generalized index (gSPRI-fNDVI) across RWC and green vegetation analyses as shown by the across-class average R^2 and *RMSE* in the last column of Table 5, supporting our selection of the 2036 nm wavelength for band 1. The combined findings of the RWC and green vegetation analyses indicate that the recommendation of band 2 at

2097 ($\pm$14 nm) is ideal and well supported. For band 3, the top-performing wavelengths range from 2154 to 2225 nm. Although this a wide range, the two top-performing band 3 wavelengths were 2216 and 2217 nm. These top-performing wavelengths are less than a 20 nm shift compared to the Landsat 8 SWIR2 band center at 2200 nm, supporting some level of mission continuity with Landsat 4–9, albeit with a narrow band width. This slight increase in wavelength for band 3 was found to be advantageous for improving f_R estimation performance in general. This supports our final selection of 2214 nm for band 3 from a top-performing wavelength range of 2110 to 2217 nm. However, like band 2, we note there is a wide range of wavelengths that will represent good performance in f_R estimation for Landsat Next with a three-band configuration for SWIR2.

Overall, what was critical to this study's focus was the consistent identification of high-performing bands at CAI-type wavelengths. The indices producing the lowest *RMSE* in f_R estimation for the combined RWC and green vegetation analysis were all three-band indices with CAI-type wavelengths (including CAI itself). Our selection of final bands centered at 2036, 2097, and 2214 nm provides three bands well-suited for resolving the 2100 nm lignocellulose absorption feature of crop residue and other NPV over a range of conditions. The selected cutoff at 2350 nm in our analysis due to spectrometer noise may have limited our ability to fully examine the 2350 to 2500 nm spectral range. It is possible that clean spectra with high SNR measurements free from artifacts may reveal a different pattern in the wavelength shift analysis for two- or three-band indices; for example, a three-band index centered on the 2300 nm absorption feature that is evidenced in NPV spectra with high SNR. However, given lower radiance levels at longer wavelengths and the influence of atmospheric water vapor, clear satellite observations of the longward edge of the 2300 nm absorption feature may be difficult to obtain with broad band multispectral sensors. While our findings comport with former studies and establish well-evidenced band selections, it is critical to note the limitations of this study, the first of which is the limited geographic extent of this study, with all spectra being acquired from fields in the same region. This study was also limited to maize, soybean, and wheat crop residue spectra. Performing a similar analysis with a more globally representative distribution of spectra could greatly improve this analysis. Second, our analysis only compared SR- and atm-processed spectra from a single atmospheric correction simulation. Before establishing finalized band placements for Landsat Next, a more detailed assessment of atmospheric impacts on f_R estimation performance is needed.

5. Conclusions

This study used a wavelength shift approach to locate optimal wavelength positions of 1 nm interval (30 nm bandwidth) multispectral bands and 10 nm hyperspectral bands for use in spectral indices estimating fractional crop residue (f_R) cover. The results of the analyses for two-band spectral indices indicate that Shortwave Infrared Normalized Difference Residue Index (SINDRI) and Shortwave Infrared Difference Residue Index (SIDRI) bands around 2210 nm and 2260 nm have good performance in f_R estimation. Wide ranges of SINDRI/SIDRI (from 2210 to 2230 for band 1 and from 2260 to 2270 for band 2) yielded high performance. We developed a novel approach with the three-band wavelength shift analysis finding that three-band generalized indices perform best in f_R estimation when bands are spectrally positioned in the Cellulose Absorption Index (CAI) region (~2040, ~2100, and ~2210 nm). The top-performing three bands across the generalized Center Peak Difference Index (gCPDI), generalized Center Peak Ratio Index (gCPRI), generalized Side Peak Ratio Index (gSPRI), and heritage CAI were found to be 2036, 2097, and 2214 nm. We found that with this three-band case for Landsat Next SWIR2 a wide range of wavelengths were acceptable for the second band (from 2085 to 2115 nm) and third band (from 2160 to 2230 nm), but the first band should be located as closely to 2036 nm as possible, as the wavelength shift analysis consistently identified 2036 ($\pm$5 nm) as a top performer in f_R estimation. It should be noted that CAI and gSPRI performed best in f_R estimation across a range of fractional green vegetation (f_{GV}) and relative water

content (RWC) categories illustrating their robust performance across a wide range of ground conditions. While the LCPCDI-type wavelengths (band 1 > 2100 nm constraint) performed comparably in f_R estimation under conditions of limited green vegetation and with varying RWC levels, CAI-type wavelengths outperformed LCPCDI-type wavelengths when moderate levels of green vegetation were present. This finding further supported our selection of 2036–2097–2214 nm CAI-type bands for Landsat Next SWIR2. Although this research effort was illustrative overall, it was limited in the sense that it did not have an assessment of the full impact of atmospheric absorption features, variability in background soils, nor a broad array of crop residue/non-photosynthetic vegetation (NPV) types. Future research on these topics could address knowledge gaps and improve crop residue and NPV characterization capabilities for Landsat Next across a wider range of conditions.

Supplementary Materials: The following supporting information can be downloaded at: https://www.mdpi.com/article/10.3390/rs14236128/s1, Figures S1–S4 provide side-by-side comparisons of SR-processed (surface reflectance) and atm-processed (surface reflectance with atmospheric artifacts) spectra fractional crop residue cover (f_R) estimation performance. Supplemental Figures S1–S4 expand on the findings presented in Figures 2 and 3 and Table 1 of the main publication. Figures S5–S8 are the rotational, interactive versions of Figure 6a,c and Figure 7a,c from the main publication. Figures S5–S8 are provided in the supplementary materials allowing further exploration of the three-band wavelength shift analysis f_R estimation performance.

Abbreviations

atm	abbreviation for spectra with atmospheric residuals
AVIRIS	Airborne Visible/Infrared Imaging Spectrometer
BARC	Beltsville Agricultural Research Center (USDA)
CAI	Cellulose Absorption Index
ETM+	Enhanced Thematic Mapper Plus (on Landsat 7)
f_{GV}	Fractional green vegetation cover
f_R	Fractional crop residue cover
f_S	Fractional soil cover
gCPDI	Generalized Center Peak Difference Index (three-band)
gCPRI	Generalized Center Peak Ratio Index (three-band)
gDI	Generalized Difference Index (two-band)
gNDI	Generalized Normalized Difference Index (two-band)

gSPRI	Generalized Side Peak Ratio Index (three-band)
LCA	Lignin Cellulose Absorption index
LCPCDI	Lignin Cellulose Peak Center Difference Index
LCPCDI$_{v2}$	Lignin Cellulose Peak Center Difference Index version 2
MSI	Multispectral Instrument (on Sentinel-2)
NDTI	Normalized Difference Tillage Index
NDVI	Normalized Difference Vegetation Index
NPV	Non-photosynthetic vegetation
OLI	Operational Land Imager (on Landsats 8 and 9)
PRISMA	PRecursore IperSpettrale della Missione Applicativa
rCAI$_{LP}$	Ratio CAI—Left Peak (two-band)
rCAI$_{RP}$	Ratio CAI—Right Peak (two-band)
RWC	Relative water content
SI	Spectral index
SIDRI	Shortwave Infrared Difference Residue Index
SINDRI	Shortwave Infrared Normalized Difference Residue Index
SR	Surface reflectance
SWIR	Shortwave infrared
SWIR1	Shorter wavelength SWIR region and band for OLI and MSI (~1600 nm)
SWIR2	Longer wavelength SWIR region and band for OLI and MSI (~2200 nm)
TM	Thematic Mapper (on Landsat 5)
WV3	WorldView-3

References

1. Wu, Z.; Snyder, G.; Vadnais, C.; Arora, R.; Babcock, M.; Stensaas, G.; Doucette, P.; Newman, T. User needs for future Landsat missions. *Remote Sens. Environ.* **2019**, *231*, 111214. [CrossRef]
2. NASA, Goddard Space Flight Center. Landsat Next Request for Information (RFI). 2020. Available online: https://sam.gov/opp/09a18f980f67449fa10608ecb0924883/view?keywords=%22Landsat%20Next%22 (accessed on 30 October 2020).
3. Lal, R. The Role of Residues Management in Sustainable Agricultural Systems. *J. Sustain. Agric.* **1995**, *5*, 51–78. [CrossRef]
4. Magdoff, F.; Weil, R. Soil Organic Matter Management Strategies. In *Soil Organic Matter in Sustainable Agriculture*; CRC Press: Boca Raton, FL, USA, 2004. [CrossRef]
5. Delgado, J.A. Crop residue is a key for sustaining maximum food production and for conservation of our biosphere. *J. Soil Water Conserv.* **2010**, *65*, 111A–116A. [CrossRef]
6. Palm, C.; Blanco-Canqui, H.; DeClerck, F.; Gatere, L.; Grace, P. Conservation agriculture and ecosystem services: An overview. *Agric. Ecosyst. Environ.* **2014**, *187*, 87–105. [CrossRef]
7. Zheng, B.; Campbell, J.B.; Serbin, G.; Daughtry, C.S.T. Multitemporal remote sensing of crop residue cover and tillage practices: A validation of the minNDTI strategy in the United States. *J. Soil Water Conserv.* **2013**, *68*, 120–131. [CrossRef]
8. Conservation Technology Information Center. *Procedures for Using the Cropland Roadside Transect Survey for Obtaining Tillage Crop Residue Data*; Conservation Technology Information Center, Purdue University: West Lafayette, IN, USA, 2009; Available online: http://www.ctic.org (accessed on 5 May 2022).
9. Masek, J.G.; Wulder, M.A.; Markham, B.; McCorkel, J.; Crawford, C.J.; Storey, J.; Jenstrom, D.T. Landsat 9: Empowering open science and applications through continuity. *Remote Sens. Environ.* **2020**, *248*, 111968. [CrossRef]
10. U.S. Geological Survey. What are the Band Designations for the Landsat Satellites? 2022. Available online: https://www.usgs.gov/faqs/what-are-band-designations-landsat-satellites (accessed on 21 May 2022).
11. Daughtry, C.S.T.; Doraiswamy, P.C.; Hunt, E.R.; Stern, A.J.; McMurtrey, J.E.; Prueger, J.H. Remote sensing of crop residue cover and soil tillage intensity. *Soil Tillage Res.* **2006**, *91*, 101–108. [CrossRef]
12. Knight, E.J.; Kvaran, G. Landsat-8 Operational Land Imager Design, Characterization and Performance. *Remote Sens.* **2014**, *6*, 10286–10305. [CrossRef]
13. ACCP. *Accelerated Canopy Chemistry Program Final Report to NASA-EOS-IWG*; National Aeronautics and Space Administration: Washington, DC, USA, 1994. Available online: http://daac.ornl.gov/ACCP/accp.html (accessed on 23 May 2022).
14. Serrano, L.; Penuelas, J.; Ustin, S.L. Remote sensing of nitrogen and lignin in Mediterranean vegetation from AVIRIS data: Decomposing biochemical from structural signals. *Remote Sens. Environ.* **2002**, *81*, 355–364. [CrossRef]
15. Kokaly, R.F.; Despain, D.G.; Clark, R.N.; Livo, K.E. Mapping vegetation in Yellowstone National Park using spectral feature analysis of AVIRIS data. *Remote Sens. Environ.* **2003**, *84*, 437–456. [CrossRef]
16. Kokaly, R.F.; Rockwell, B.W.; Haire, S.L.; King, T.V. Characterization of post-fire surface cover, soils, and burn severity at the Cerro Grande Fire, New Mexico, using hyperspectral and multispectral remote sensing. *Remote Sens. Environ.* **2007**, *106*, 305–325. [CrossRef]
17. Pepe, M.; Pompilio, L.; Gioli, B.; Busetto, L.; Boschetti, M. Detection and Classification of Non-Photosynthetic Vegetation from PRISMA Hyperspectral Data in Croplands. *Remote Sens.* **2020**, *12*, 3903. [CrossRef]

18. Van Deventer, A.P.; Ward, A.D.; Gowda, P.M.; Lyon, J.G. Using thematic mapper data to identify contrasting soil plains and tillage practices. *Photogramm. Eng. Remote Sens.* **1997**, *63*, 87–93.

19. Jin, X.; Ma, J.; Wen, Z.; Song, K. Estimation of maize residue cover using Landsat-8 OLI image spectral information and textural features. *Remote Sens.* **2015**, *7*, 14559–14575. [CrossRef]

20. Hively, W.D.; Lamb, B.T.; Daughtry, C.S.T.; Shermeyer, J.; McCarty, G.W.; Quemada, M. Mapping crop residue and tillage intensity using WorldView-3 satellite shortwave infrared residue indices. *Remote Sens.* **2018**, *10*, 1657. [CrossRef]

21. Najafi, P.; Navid, H.; Feizizadeh, B.; Eskandari, I.; Blaschke, T. Fuzzy object-based image analysis methods using Sentinel-2A and Landsat-8 data to map and characterize soil surface residue. *Remote Sens.* **2019**, *11*, 2583. [CrossRef]

22. Azzari, G.; Grassini, P.; Edreira, J.I.R.; Conley, S.; Mourtzinis, S.; Lobell, D.B. Satellite mapping of tillage practices in the North Central US region from 2005 to 2016. *Remote Sens. Environ.* **2019**, *221*, 417–429. [CrossRef]

23. Beeson, P.C.; Daughtry, C.S.T.; Wallander, S.A. Estimates of conservation tillage practices using Landsat archive. *Remote Sens.* **2020**, *12*, 2665. [CrossRef]

24. Hagen, S.C.; Delgado, G.; Ingraham, P.; Cooke, I.; Emery, R.; Fisk, J.P.; Melendy, L.; Olson, T.; Patti, S.; Rubin, N.; et al. Mapping conservation management practices and outcomes in the corn belt using the operational tillage information system (Optis) and the denitrification–decomposition (DNDC) model. *Land* **2020**, *9*, 408. [CrossRef]

25. Yue, J.; Tian, Q.; Dong, X.; Xu, N. Using broadband crop residue angle index to estimate the fractional cover of vegetation, crop residue, and bare soil in cropland systems. *Remote Sens. Environ.* **2020**, *237*, 111538. [CrossRef]

26. Yue, J.; Fu, Y.; Guo, W.; Feng, H.; Qiao, H. Estimating fractional coverage of crop, crop residue, and bare soil using shortwave infrared angle index and Sentinel-2 MSI. *Int. J. Remote Sens.* **2022**, *43*, 1253–1273. [CrossRef]

27. South, S.; Qi, J.; Lusch, D.P. Optimal classification methods for mapping agricultural tillage practices. *Remote Sens. Environ.* **2004**, *91*, 90–97. [CrossRef]

28. Bannari, A.; Pacheco, A.; Staenz, K.; McNairn, H.; Omari, K. Estimating and mapping crop residues cover on agricultural lands using hyperspectral and IKONOS data. *Remote Sens. Environ.* **2006**, *104*, 447–459. [CrossRef]

29. Yue, J.; Tian, Q.; Dong, X.; Xu, K.; Zhou, C. Using hyperspectral crop residue angle index to estimate maize and winter-wheat residue cover: A laboratory study. *Remote Sens.* **2019**, *11*, 807. [CrossRef]

30. Daughtry, C.S.T.; Hunt, E.R. Mitigating the effects of soil and residue water contents on remotely sensed estimates of crop residue cover. *Remote Sens. Environ.* **2008**, *112*, 1647–1657. [CrossRef]

31. Serbin, G.; Daughtry, C.S.T.; Hunt, E.R.; Brown, D.J.; McCarty, G.W. Effect of Soil Spectral Properties on Remote Sensing of Crop Residue Cover. *Soil Sci. Soc. Am. J.* **2009**, *73*, 1545–1558. [CrossRef]

32. Quemada, M.; Hively, W.D.; Daughtry, C.S.T.; Lamb, B.T.; Shermeyer, J. Improved crop residue cover estimates obtained by coupling spectral indices for residue and moisture. *Remote Sens. Environ.* **2018**, *206*, 33–44. [CrossRef]

33. Anderegg, W.R.L.; Anderegg, L.D.L.; Huang, C.Y. Testing early warning metrics for drought-induced tree physiological stress and mortality. *Glob. Chang. Biol.* **2019**, *25*, 2459–2469. [CrossRef]

34. Coates, A.R.; Dennison, P.E.; Roberts, D.A.; Roth, K.L. Monitoring the impacts of severe drought on Southern California chaparral species using hyperspectral and thermal infrared imagery. *Remote Sens.* **2015**, *7*, 14200–14215. [CrossRef]

35. Bai, X.; Zhao, W.; Ji, S.; Qiao, R.; Dong, C.; Chang, X. Estimating fractional cover of non-photosynthetic vegetation for various grasslands based on CAI and DFI. *Ecol. Indic.* **2021**, *131*, 108252. [CrossRef]

36. Lugassi, R.; Chudnovsky, A.; Zaady, E.; Dvash, L.; Goldshleger, N. Spectral Slope as an Indicator of Pasture Quality. *Remote Sens.* **2015**, *7*, 256–274. [CrossRef]

37. Hively, W.D.; Lamb, B.T.; Daughtry, C.S.T.; Serbin, G.; Dennison, P.; Kokaly, R.F.; Wu, Z.; Masek, J.G. Evaluation of SWIR crop residue bands for the Landsat Next mission. *Remote Sens.* **2021**, *13*, 3718. [CrossRef]

38. Kokaly, R.F.; Asner, G.P.; Ollinger, S.V.; Martin, M.E.; Wessman, C.A. Characterizing canopy biochemistry from imaging spectroscopy and its application to ecosystem studies. *Remote Sens. Environ.* **2009**, *113*, S78–S91. [CrossRef]

39. Dennison, P.E.; Qi, Y.; Meerdink, S.K.; Kokaly, R.F.; Thompson, D.R.; Daughtry, C.S.T.; Quemada, M.; Roberts, D.A.; Gader, P.D.; Wetherley, E.B.; et al. Comparison of methods for modeling fractional cover using simulated satellite hyperspectral imager spectra. *Remote Sens.* **2019**, *11*, 2072. [CrossRef]

40. Quemada, M.; Daughtry, C.S.T. Spectral indices to improve crop residue cover estimation under varying moisture conditions. *Remote Sens.* **2016**, *8*, 660. [CrossRef]

41. Serbin, G.; Hunt, E.R.; Daughtry, C.S.T.; McCarty, G.W.; Doraiswamy, P.C. An improved ASTER index for remote sensing of crop residue. *Remote Sens.* **2009**, *1*, 971–991. [CrossRef]

42. Elvidge, C.D. Visible and near infrared reflectance characteristics of dry plant materials. *Int. J. Remote Sens.* **1990**, *11*, 1775–1795. [CrossRef]

43. Nagler, P.L.; Daughtry, C.S.T.; Goward, S.N. Plant litter and soil reflectance. *Remote Sens. Environ.* **2000**, *71*, 207–215. [CrossRef]

44. Daughtry, C.S.T.; Hunt, E.R.; Doraiswamy, P.C.; McMurtrey, J.E. Remote sensing the spatial distribution of crop residues. *Agron. J.* **2005**, *97*, 864–871. [CrossRef]

45. Prabhakara, K.; Hively, W.D.; McCarty, G.W. Evaluating the relationship between biomass, percent groundcover and remote sensing indices across six winter cover crop fields in Maryland, United States. *Int. J. Appl. Earth Obs. Geoinf.* **2015**, *39*, 88–102. [CrossRef]

46. Philpot, W.; Jacquemoud, S.; Tian, J. ND-space: Normalized difference spectral mapping. *Remote Sens. Environ.* **2021**, *264*, 112622. [CrossRef]
47. Wang, L.; Hunt, E.R., Jr.; Qu, J.J.; Hao, X.; Daughtry, C.S.T. Remote sensing of fuel moisture content from ratios of narrow-band vegetation water and dry-matter indices. *Remote Sens. Environ.* **2013**, *129*, 103–110. [CrossRef]
48. Thoma, D.P.; Gupta, S.C.; Bauer, M.E. Evaluation of optical remote sensing models for crop residue cover assessment. *J. Soil Water Conserv.* **2004**, *59*, 224–233.
49. Hively, W.D.; Lamb, B.T.; Daughtry, C.S.T.; Serbin, G.; Dennison, P. *Reflectance Spectra of Agricultural Field Conditions Supporting Remote Sensing Evaluation of Non-Photosynthetic Vegetative Cover (version 1.1)*; U.S. Geological Survey: Reston, VI, USA, 2021. [CrossRef]